PERGAMON

Applied Geochemistry 15 (2000) 1219–1244

Applied Geochemistry

www.elsevier.com/locate/apgeochem

Arsenic speciation in pyrite and secondary weathering phases, Mother Lode Gold District, Tuolumne County, California

Kaye S. Savage[a,*], Tracy N. Tingle[a,1], Peggy A. O'Day[b], Glenn A. Waychunas[c], Dennis K. Bird[a]

[a]*Department of Geological and Environmental Sciences, Stanford University, Stanford, CA 94305, USA*
[b]*Department of Geology, Arizona State University, Tempe, AZ, 85287-1404, USA*
[c]*Lawrence Berkeley National Laboratory, Berkeley, CA, 94720, USA*

Received 13 April 1999; accepted 15 November 1999
Editorial handling by J.S. Herman

Abstract

Arsenian pyrite, formed during Cretaceous gold mineralization, is the primary source of As along the Melones fault zone in the southern Mother Lode Gold District of California. Mine tailings and associated weathering products from partially submerged inactive gold mines at Don Pedro Reservoir, on the Tuolumne River, contain ~20–1300 ppm As. The highest concentrations are in weathering crusts from the Clio mine and nearby outcrops which contain goethite or jarosite. As is concentrated up to 2150 ppm in the fine-grained (< 63 μm) fraction of these Fe-rich weathering products.

Individual pyrite grains in albite-chlorite schists of the Clio mine tailings contain an average of 1.2 wt.% As. Pyrite grains are coarsely zoned, with local As concentrations ranging from ~0 to 5 wt.%. Electron microprobe, transmission electron microscope, and extended X-ray absorption fine-structure spectroscopy (EXAFS) analyses indicate that As substitutes for S in pyrite and is not present as inclusions of arsenopyrite or other As-bearing phases. Comparison with simulated EXAFS spectra demonstrates that As atoms are locally clustered in the pyrite lattice and that the unit cell of arsenian pyrite is expanded by ~2.6% relative to pure pyrite. During weathering, clustered substitution of As into pyrite may be responsible for accelerating oxidation, hydrolysis, and dissolution of arsenian pyrite relative to pure pyrite in weathered tailings. Arsenic K-edge EXAFS analysis of the fine-grained Fe-rich weathering products are consistent with corner-sharing between As(V) tetrahedra and Fe(III)-octahedra. Determinations of nearest-neighbor distances and atomic identities, generated from least-squares fitting algorithms to spectral data, indicate that arsenate tetrahedra are sorbed on goethite mineral surfaces but substitute for SO_4 in jarosite. Erosional transport of As-bearing goethite and jarosite to Don Pedro Reservoir increases the potential for As mobility and bioavailability by desorption or dissolution. Both the substrate minerals and dissolved As species are expected to respond to seasonal changes in lake chemistry caused by thermal stratification and turnover within the monomictic Don Pedro Reservoir. Arsenic is predicted to be most bioavailable and toxic in the reservoir's summer hypolimnion.

* Corresponding author. Tel.: +1-650-723-8017; fax: +1-650-725-0979.
E-mail address: savage@pangea.stanford.edu (K.S. Savage).
[1] Deceased, 1996.

0883-2927/00/$ - see front matter
PII: S0883-2927(99)00115-8

1. Introduction

Concern over toxic metals in ground and surface waters has led to increased interest in the geochemistry of weathering mine waste. In the Mother Lode District of California, As is released to the environment by weathering of As-rich sulfides concentrated in surface accumulations from mine operations. As the popu-

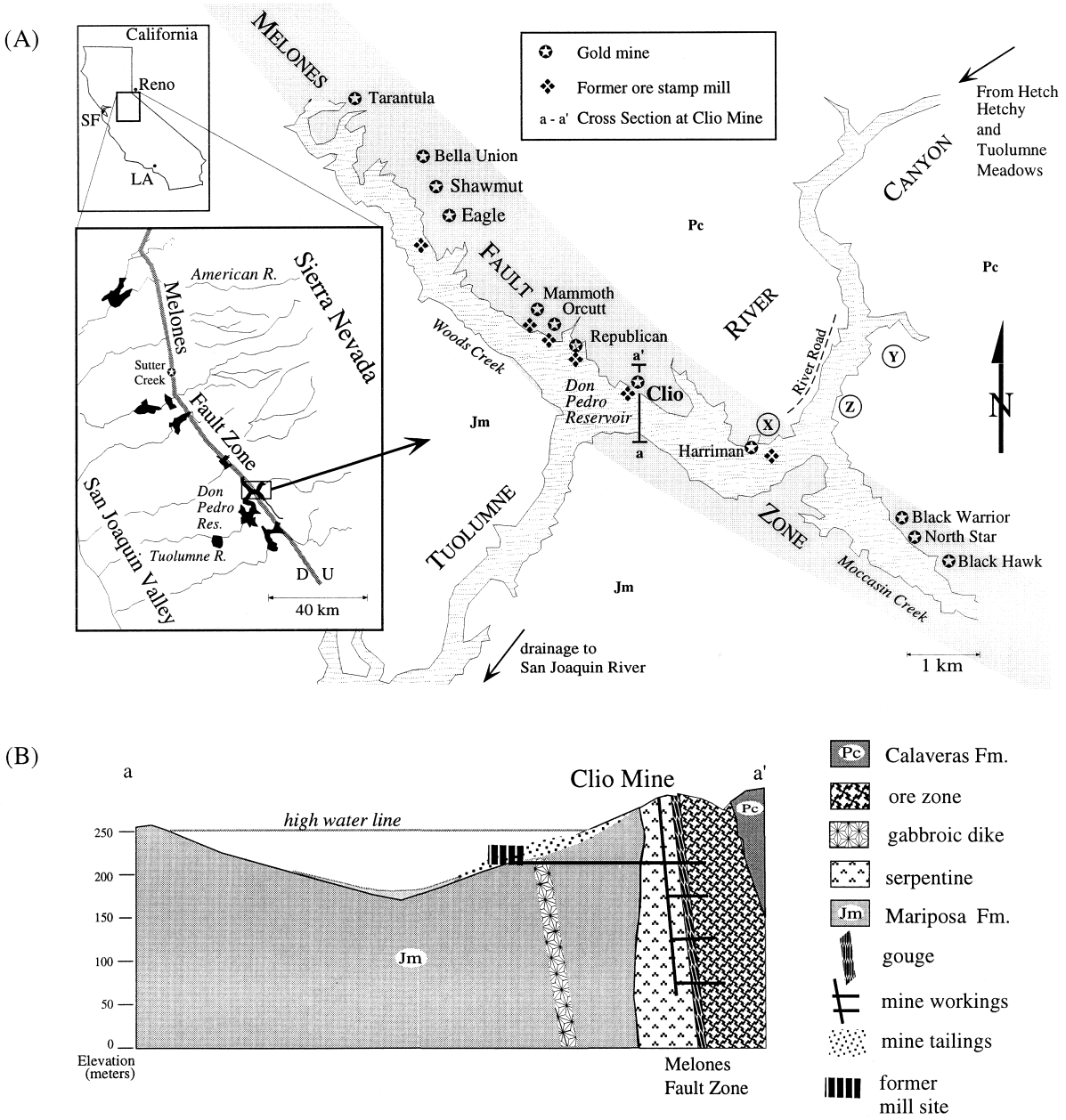

Fig. 1. (A) Location map showing the study area in relation to the Sierra Nevada lode gold mining area and major rivers crossing the Melones fault zone. Mine locations from Parsons (1920) and Knopf (1929). (B) Geologic cross section across the Melones fault zone in the vicinity of the Clio mine, modified from Knopf (1929) to show the location of Don Pedro Reservoir and tailings of the Clio mine.

lation of California increases, demand for drinking and irrigation water from upland regions and development of foothill areas previously used for mining continue to rise, increasing the risk of human exposure to high As concentrations. One example is the residential Mesa de Oro subdivision of Sutter Creek (Fig. 1A, inset), where homes were constructed on mine tailings and soils of the Central Eureka Mine containing up to ~1300 ppm As (Walker et al., 1994). In addition to soil contamination, chemical reactions between mine waste and river or lake waters can lead to elevated concentrations of dissolved As (cf. Azcue et al., 1994; Harrington et al., 1998). The maximum contaminant level (MCL) for As in drinking water is under review by the US Environmental Protection Agency. The current MCL of 50 μg/l is mandated to be revised by 1 January 2001, probably in the range of 2–20 μg/l (Pontius, 1995). This change in regulation will impact many public water supplies in California and impose a significant economic burden by forcing treatment of waters in systems that are currently in compliance. Thus, understanding the natural sources of As in California, its mobility and accumulation in the environment, its removal from solution by sediments and biota, and its chemistry and speciation in solid phases are key elements in limiting As exposure to humans and mitigating its migration into natural waters.

In this study, the geochemical cycling of As is examined by employing a variety of analytical methods that characterize As concentration, distribution, speciation, and bonding from the field to molecular scale. The study concentrates on mineralized outcrops and tailings near Don Pedro Reservoir (Fig. 1A) and the Clio Mine (cross section, Fig. 1B) in the southern part of the Mother Lode Gold Mining District. Here, As-bearing sulfides exposed to atmospheric weathering (oxidizing conditions) produce fine-grained, secondary Fe(III) oxides/hydroxides (goethite, ferrihydrite) and sulfates (jarosite) that form 'weathering crusts' during periods of low rainfall (cf. Bowell, 1994). These Fe(III)-rich weathering products, which are efficacious scavengers of As oxyanions (Pierce and Moore, 1980; Aggett and O'Brien, 1985; Peterson and Carpenter, 1986), contain up to ~2000 ppm As. The present study employs bulk chemical (X-ray fluorescence; inductively-coupled plasma atomic emission spectroscopy) and mineralogical (electron probe microanalysis; X-ray diffraction; transmission electron microscopy) analyses to characterize the distribution of As in rocks, sulfide minerals (arsenian pyrite) and secondary phases produced during weathering (goethite and jarosite). The atomic speciation of As in arsenian pyrite, goethite, and jarosite is determined by synchrotron X-ray absorption spectroscopy and extended X-ray absorption fine structure spectroscopy (EXAFS) analysis. Relatively few studies to date have applied EXAFS spectroscopy to complex natural geologic samples, but it is an effective, element-specific tool for identifying the speciation of environmental contaminants (Manceau et al., 1996; Foster et al., 1998; O'Day et al., 1998; Morin et al., 1999; Ostergren et al., 1999). By using multiple techniques to understand As geochemistry in the mine waste environment, the speciation of As is tracked through weathering processes and its fate is anticipated in the aquatic environment of the monomictic Don Pedro Reservoir.

1.1. Geologic and environmental background

The historically famous Mother Lode Gold District of California extends for 225 km along the western Sierra Nevada foothills. Most of the Gold deposits formed within a folded and faulted metamorphic belt of lower greenschist to amphibolite facies sedimentary and igneous rocks 110–140 Ma ago (Kistler et al., 1983; Bohlke and Kistler, 1986). In the southern portion of the Mother Lode Gold District (Fig. 1A) many lode gold ores are associated with the Melones fault zone (MFZ), which separates a Jurassic oceanic crust complex to the west from Paleozoic metavolcanic and metasedimentary rocks to the east. The lodes are characterized by quartz veins and carbonate rocks formed by metasomatic reactions of mineralizing fluids with greenschist facies rocks at temperatures between 250 and 325°C (Weir and Kerrick, 1987). Ore-forming fluids introduced CO_2, S, and K_2O (Knopf 1929; Kistler et al., 1983; Landefeld and Snow, 1990), overprinting an earlier Na_2O metasomatic event (Landefeld and Snow, 1990). Tertiary uplift exposed and eroded the gold-bearing veins, forming placer deposits that were subsequently blanketed by Eocene volcanic rocks (Knopf, 1929). Continued uplift and erosion exposed the Tertiary placers and the underlying mineralized bedrock, forming modern placers whose discovery led to California's famous gold rush.

Since the 1848 discovery of gold near the confluence of Woods and Moccasin Creeks with the Tuolumne River (Fig. 1A), this region of the Mother Lode has produced greater than 4 million tons of processed ore tailings (Wagner, 1970). Unlike other Mother Lode deposits that typically contain several % total sulfide, ores in this region are sulfide-rich. The "sulfide ore," with up to 15% total sulfides, consists of fine-grained blackish-green chlorite schist, locally replaced by pyrite and Ca-Mg-Fe carbonates (Knopf, 1929). Pyrite is the most abundant sulfide, and arsenopyrite is rare (Knopf, 1929).

In the study area, mines are concentrated along the Moccasin and Woods Creek drainages that are now partially flooded by the Don Pedro Reservoir on the Tuolumne River (Fig. 1A). The Melones fault zone

(see cross-section in Fig. 1B) is a structurally complex melange of metashales, metavolcanic rocks, clastic sediments, carbonates (both limestone and dolomite), diorite, and metamorphosed mafic and ultramafic rocks, all of which have experienced varying grades of metamorphism, tectonism, and later metasomatism during gold mineralization. Waste materials produced during mining operations are heterogeneous piles of rocks that have undergone varying degrees of crushing, granulation, and chemical processing. They are mineralogically complex chemical reactors that interact with the atmosphere and with lake waters of Don Pedro Reservoir, which seasonally floods many of the mine and mill sites of the Tuolumne River Canyon.

2. Methods

2.1. Bulk sample characterization

Seventeen whole rock samples and 28 samples of sediments and fine-grained weathering products of tailings and outcrops (Table 1) were analyzed by bulk chemical methods (see footnotes Tables 2, 5 and 6). Microprobe analyses of sulfides, silicates, and carbonates were conducted at Stanford University (see footnote a of Table 3). Mineral identification of weathering product samples was conducted by X-ray diffraction at Stanford University (see footnote c of Table 5). Imaging by high-resolution transmission electron microscopy (HR-TEM) was conducted at Arizona State University using techniques described by Dódony et al. (1996).

Two samples of secondary weathering crusts were analyzed for surface area and particle size distribution. Surface areas of 230–250 mg subsamples screened to <63 μm were measured using the N_2-BET method with a Coulter SA 3100 gas adsorption BET analyzer. Particle size determinations were conducted on a Coulter LS230 laser diffraction size analyzer after ultrasonic disaggregation of 250 mg sample in 10 ml purified (MilliQ) water.

2.2. X-ray absorption spectroscopy (XAS)

A pyrite sample from the Clio mine (separated from sample Clio-2) and two pyrite weathering products, goethite (DP-011) and jarosite (DP-045) were studied by XAS. Arsenic K-edge absorption spectra were collected at the Stanford Synchrotron Radiation Laboratory (SSRL) on wiggler beamline 4-3 at cryogenic temperature (~10 K) under dedicated conditions (3 GeV, 70–90 mA) using an unfocused beam. Samples were diluted with inert $B(OH)_3$ (75% for Clio-2, 50% for DP-011, none for DP-045) to reduce high background fluorescence from Fe. Powdered samples were loaded into 2-mm-thick teflon sample holders and sealed with Mylar film. Arsenic K-edge (11,867 eV) and EXAFS spectra were collected using Si(111) monochromator crystals for Clio-2 and DP011 and a Si (220) crystal for DP-045. Fluorescence spectra were collected with a 13-element solid-state Ge-fluorescence array detector; total count rate was reduced with 250-μm-thick Al-foil filters. Beam energy was calibrated on As foil at 11,867 eV. Energy scans from 11,650–12,745 eV ($k = 15$ Å^{-1}) were collected and averaged ($N = 7$ for Clio-2; $N = 17$ for DP-011, $N = 4$ for DP-045) for each sample. Data collection of solid reference compound spectra is described in Foster et al. (1998) for arsenopyrite and Waychunas et al. (1993) for scorodite (both sets of data collected at room temperature).

Iron K-edge absorption spectra for DP-011, DP-045, and a synthetic goethite reference compound (prepared by Dr John Bargar using method of Van Geen et al. (1994)) were collected on SSRL wiggler beamline 4-1 in transmission mode using Si(111) (for DP-011 and goethite) and Si(220) (for DP-045) monochromator crystals and gas-filled ion chambers (N_2 in I_0, I_1 and Ar in I_2). Thin (~0.2 mm) layers of powdered sample were evenly smeared on adhesive tape and stacked together to attain 2 mm total sample thickness. Three energy scans from 6900 to 7750 eV ($k = 13$ Å^{-1}) were collected at room temperature and averaged for each sample. Energy was calibrated using the Fe foil edge inflection point at 7111 eV. For all spectra, harmonic rejection was achieved by detuning the monochromator to reduce the incident beam intensity by 30–50% of its maximum measured in the first ionization chamber (I_0).

Numerical results were extracted from the EXAFS spectra using a curved-wave formalism and a single-scattering approximation implemented in the computer code EXAFSPAK (George and Pickering, 1993). Background below the absorption edge was estimated by a linear fit through the pre-edge region; background above the edge was estimated by fitting a cubic spline with three to four segments. Spectra were normalized using the edge-step height near the absorption edge, extrapolated through the XAFS region using a Victoreen polynomial and tabulated McMaster coefficients (McMaster et al., 1969), and weighted by k^3. Spectra were fitted with theoretical phase-shift and amplitude reference functions calculated by the ab initio computer code FEFF6 (Rehr et al., 1992; Rehr, 1993) using atomic clusters generated from the crystal structures of arsenopyrite (FeAsS), pyrite (FeS_2) with As substituted for S as the central absorber, scorodite ($FeAsO_4{\cdot}2H_2O$), goethite (α-FeOOH), and jarosite ($KFe_3(SO_4)_2(OH)_6$). Initially, filtered XAFS spectra of individual peaks in the radial structure functions (RSF) generated by Fourier transform were fitted with

Table 1
Descriptions and locations for bulk chemistry[a]

Sample	Location (Fig. 1A)	Type
Rocks and tailings		
Clio-1	Clio (T)	Pyrite-bearing albite-chlorite schist
Clio-2	Clio (T)	Pyrite-bearing albite-chlorite schist (see text)
Clio-3	Clio (T)	Pyrite-bearing albite-chlorite schist
DP-007	X (O)	Black laminated slate
DP-034	X (O)	Serpentinized harzburgite
DP-040	Z (O)	Albitite dike
DP-051	Y (O)	Slate of Calaveras Fm
DP-082	X (O)	Black laminated slate, MFZ
DP-114	Clio (T)	Pyrite-bearing albite-chlorite schist
DP-115	Clio (T)	Pyrite-bearing chloritic slate
DP-116	Clio (T)	Pyrite-bearing albite-chlorite schist
DP-117	Clio (T)	Pyrite-bearing chloritic slate (pyrite weathered out)
DP-118	Clio (T)	Pyrite-bearing albite-chlorite schist
DP-119	Clio (T)	Pyrite-bearing albite-chlorite schist
DP-120	Clio (T)	Quartz-veined serpentine
DP-121	Clio (S)	Iron-stained mica schist pebble in sediment
DP-123	Clio (T)	Pyrite-bearing albite-chlorite schist
Soils, sediment and weathering products		
DP-001	X	Jarosite-rich weathering crust, MFZ
DP-011	Clio (F)	Goethite-rich weathering crusts (see text)
DP-025	X	Red soil developed on slate of Calaveras Fm
DP-030	X	Jarosite-rich weathering product, MFZ
DP-038	Y	Iron oxide matrix of breccia at Giant Lode
DP-043	X	Clay-rich sediment, MFZ
DP-044	X	Colluvium below sulfide-rich ultramafic rock, MFZ
DP-045	X	Jarosite-rich weathering product, MFZ (see text)
DP-046	X	Tan sediment, MFZ
DP-047	X	Colluvium below ultramafic rock, MFZ
DP-050	Clio (S)	Sediment
DP-052	Clio (S)	Sediment
DP-053	Clio (S)	Sediment
DP-054	Clio (S)	Soil
DP-055	Clio (S)	Reddish sediment
DP-056	Clio (S)	Soil
DP-057	WF (S)	Sediment
DP-067	X (S)	Sediment
DP-074	X	Jarosite-rich weathering product, MFZ
DP-075	X	Jarosite-rich weathering product, MFZ
DP-080	X	Pyrite-bearing colluvium, MFZ
DP-081	X	Gypsum-bearing sediment, MFZ
DP-111	Clio (T)	Goethite-rich weathering crust coating ultramafic rock
DP-112	Clio (T)	Breccia of serpentine and slate with goethite-rich matrix
DP-113	Clio (T)	Breccia of serpentine and slate with goethite-rich matrix
DP-122	Clio (T)	Brecciated, iron-stained chloritic slate
DP-124	Clio (T)	Brecciated, iron-stained chloritic slate
DP-TNT	Clio (S)	Sediment

[a] See Fig. 1A for location names. Bold numbers indicate samples used for EXAFS analysis. MFZ denotes Melones fault zone; WF denotes Wards Ferry Bridge, located 2 km east of NE map corner of Fig. 1A; (T) denotes tailings pile; (O) denotes outcrop; (F) denotes stamp mill foundation; (S) denotes reservoir shoreline.

Table 2
Chemical analyses of rocks within and near the Clio Mine (see Fig. 1A) and NNE of the Melones fault zone[a]

	Clio-2	DP-007	DP-012	DP-014	DP-034	DP-040	DP-051	DP-082	DP-114	DP-115	DP-116	DP-117	DP-118	DP-119	DP-120	DP-121	DP-123
Rock type[b]	acs	bs	acs	acs	sh	ad	cs	bs	acs	gs	acs	gs	acs	acs	s	sp	acs
Al_2O_3, %	14.98	na	17.04	na	na	18.74	5.54	na	14.98	13.63	15.23	17.45	15.12	16.06	3.62	14.18	14.09
CaO, %	6.65	na	6.05	na	na	0.88	0.23	na	6.10	5.60	6.54	5.04	2.77	5.86	5.00	12.83	6.32
Cr_2O_3, %	< 0.01	na	< 0.01	na	na	< 0.01	< 0.01	na	< 0.01	0.03	< 0.01	< 0.01	< 0.01	< 0.01	0.12	< 0.01	< 0.01
Fe_2O_3, %	9.64	na	9.54	na	na	1.75	4.41	na	5.60	10.90	6.02	9.41	10.65	9.70	7.58	9.28	7.62
K_2O, %	0.70	na	2.92	na	na	0.30	1.19	na	0.16	0.05	0.33	2.46	0.06	0.05	0.05	0.36	0.06
MgO, %	5.17	na	5.70	na	na	0.51	1.70	na	3.43	11.17	3.34	3.92	7.02	8.54	31.04	5.06	3.49
MnO, %	0.23	na	0.17	na	na	0.03	0.12	na	0.15	0.15	0.14	0.26	0.12	0.19	0.32	0.17	0.12
Na_2O, %	5.42	na	2.90	na	na	11.02	< 0.01	na	7.57	2.99	7.21	3.79	5.67	5.67	0.01	1.79	7.12
P_2O_5, %	0.40	na	0.28	na	na	0.03	0.05	na	0.02	0.31	0.05	0.28	0.24	< 0.01	0.11	0.10	0.02
SiO_2, %	46.99	na	44.81	na	na	64.41	82.72	na	52.50	44.81	53.77	49.23	51.07	45.22	32.56	53.80	51.01
TiO_2, %	0.64	na	0.77	na	na	0.18	0.30	na	0.75	0.91	0.67	0.71	0.70	0.71	0.43	0.42	0.80
LOI, %	8.22	na	6.32	na	na	0.71	2.24	na	4.68	8.14	4.84	6.14	5.59	6.55	18.14	1.21	5.43
Total, %	99.04	na	96.50	na	na	98.56	98.50	na	95.94	98.69	98.14	98.69	99.01	98.55	98.98	99.20	96.08
V, ppm	197	125	274	31	44	36	51	7	60	285	82	262	250	287	84	246	71
Cr, ppm	127	84	74	61	1580	67	111	111	73	441	91	63	138	117	634	165	75
Mn, ppm	1530	734	1225	1060	575	205	865	29	1005	1050	990	1770	820	1300	2290	1250	845
Fe, %	5.63	3.93	6.06	4.49	5.33	1.23	3.00	1.70	3.42	6.43	3.54	5.66	6.35	5.68	4.80	5.67	4.76
Co, ppm	24	17	28	11	100	2	9	4	16	31	11	27	34	28	46	26	17
Ni, ppm	14	69	23	6	2470	4	25	24	42	275	38	20	23	25	849	30	27
Cu, ppm	148	82	130	103	20	5	38	31	11	16	12	174	180	313	21	21	90
Zn, ppm	64	214	186	42	21	10	56	20	50	108	68	102	68	78	40	82	72
As, ppm	600	118	10	425	3	2	2	80	82	80	172	40	116	112	18	4	442
Sr, ppm	219	107	378	266	2	204	17	18	219	219	230	161	85	168	110	234	197
Mo, ppm	< 1	7	< 1	1	< 1	< 1	< 1	11	435	1	133	2	2	1	< 1	2	< 1
Ba, ppm	230	75	410	4	20	120	480	14	50	40	80	580	10	20	< 10	150	40
Pb, ppm	< 2	10	< 2	< 2	< 2	6	6	16	22	4	10	4	< 2	< 2	< 2	< 2	< 2

[a] Sample descriptions and locations are given in Table 1. Major element analysis (upper section of table) by X-ray fluorescence at Chemex Laboratories, Sparks, NV. Trace elements (lower section of table): As by hydride-generation atomic absorption spectroscopy at Chemex Laboratories except samples DP-007, -014, -082. Arsenic for DP-007, -014, -082 by ICP-AES at XRAL Laboratories, Don Mills, Ontario, Canada. Other elements by ICP-AES at Chemex Laboratories except samples DP-007, -014, -082. Pb for samples DP-007 and -014 by XRF at XRAL Laboratories. Other elements for samples DP-007, -014, -082 by ICP-AES at XRAL Laboratories. na, sample was not analyzed.

[b] acs, albite-chlorite schist; sh, serpentinized harzburgite; ad, albitite dike; cs, slate of Calaveras Formation; bs, black slate; s, serpentine; sp, schist pebble, gs. green chloritic slate.

Table 3
Representative electron microprobe analyses of pyrite compositions[a]

Shawmut Mine								
Sample No.	8215.2	St. Dev.	8215.4	St. Dev.	8215.8	St. Dev.	8215.10	St. Dev.
No. analyses	7		9		5		4	
Fe	45.96	0.33	46.22	0.46	46.65	0.10	46.04	0.27
S	50.69	1.39	51.83	0.94	52.73	0.39	51.68	1.18
As	2.12	0.53	2.00	0.34	1.21	0.37	1.81	0.46
Zn	0.00	0.01	0.01	0.01	0.01	0.02	0.02	0.02
Pb	0.09	0.15	0.05	0.09	0.05	0.07	0.24	0.19
Mn	0.00	0.00	0.00	0.01	0.00	0.00	0.01	0.01
Sb	0.01	0.01	0.01	0.01	0.00	0.01	0.00	0.00
Cu	0.00	0.01	0.01	0.02	0.00	0.00	0.00	0.00
Bi	0.00	0.00	0.00	0.00	0.02	0.03	0.00	0.00
Co	0.09	0.06	0.05	0.02	0.05	0.01	0.05	0.03
Ag	0.02	0.02	0.02	0.03	0.01	0.02	0.02	0.02
Ni	0.00	0.01	0.02	0.02	0.01	0.02	0.01	0.01
Au	0.02	0.03	0.01	0.02	0.03	0.06	0.01	0.02
Totals	99.02		100.22		100.77		99.88	
Clio Mine tailings pile								
Sample No.	Clio-1.3	St. Dev.	Clio-2.5	St. Dev.	Clio-2.19	St. Dev.	Clio-3.14	St. Dev.
No. analyses	3		6		5		2	
Fe	46.63	0.41	45.42	0.26	46.82	0.30	47.48	0.17
S	53.21	0.10	52.58	1.57	52.04	0.33	52.77	0.28
As	0.03	0.05	1.36	0.26	1.67	0.48	0.01	0.01
Zn	0.00	0.00	0.01	0.01	0.00	0.01	0.00	0.00
Pb	0.00	0.00	0.12	0.10	0.16	0.06	0.08	0.10
Mn	0.00	0.00	0.01	0.01	0.01	0.01	0.00	0.00
Sb	0.00	0.00	0.00	0.00	0.00	0.00	0.01	0.02
Cu	0.01	0.01	0.01	0.02	0.00	0.01	0.00	0.00
Bi	0.00	0.00	0.03	0.04	0.00	0.00	0.00	0.00
Co	0.21	0.17	0.07	0.05	0.07	0.02	0.04	0.01
Ag	0.02	0.03	0.01	0.02	0.02	0.02	0.08	0.00
Ni	0.12	0.02	0.02	0.04	0.02	0.01	0.03	0.00
Au	0.01	0.01	0.00	0.00	0.01	0.01	0.00	0.00
Totals	100.24		99.64		100.82		100.50	

[a] Compositions are an average of two to nine analyses per pyrite grain as indicated below each sample number. Analyses conducted on a JOEL 733 fully automated Superprobe with 5 wavelength dispersive spectrometers. Operating conditions were 15 keV acceleration potential and 50 nA beam current, with a spot size of 1 μm. Count times were 1 s. Data acquisition utilized the MAN background correction procedure of Donovan and Tingle (1996). Background-corrected X-ray intensity measurements were analyzed using a ZAF/phi-rho-Z matrix correction procedure (Pouchou and Pichoir, 1985). Detection limits for Fe, S and As were approximately 0.1 wt.%. Synthetic sulfide standards were from the Czamanske collection (US Geological Survey).

FEFF reference functions to determine backscatterer identities and interatomic distances. Coordination numbers for model compounds were held constant but distances and Debye–Waller factors (σ^2) were allowed to vary for each atomic shell during performance of the fitting algorithm. Final fits were done on the full, normalized spectra (k = 2.5–15 $Å^{-1}$) to remove the effects of finite window width in back Fourier transformation.

3. Results

3.1. Bulk rock chemistry and mineralogy

Bulk chemical analyses of 17 pyrite-bearing rocks (Table 1) representative of the major rock types in Fig. 1B are given in Table 2. Concentration of total As ranges from 2 to 600 ppm and is graphically represented in Fig. 2A as a function of total Fe concentration (wt.%). The lowest concentrations of As (2 ppm) were measured in two samples collected north of the Melones fault zone in pyrite-bearing slates of the Calaveras Formation (DP-051) and in albitite dikes (DP-040). Outcrops of serpentinized harzburgite (DP-034) and laminated black slate (DP-082) within the Melones fault zone (point X, Fig. 1A) contain higher As concentrations of 3 and 80 ppm, respectively. The highest bulk rock As concentrations were measured in the rocks of the Clio Mine tailings. Serpentinites and

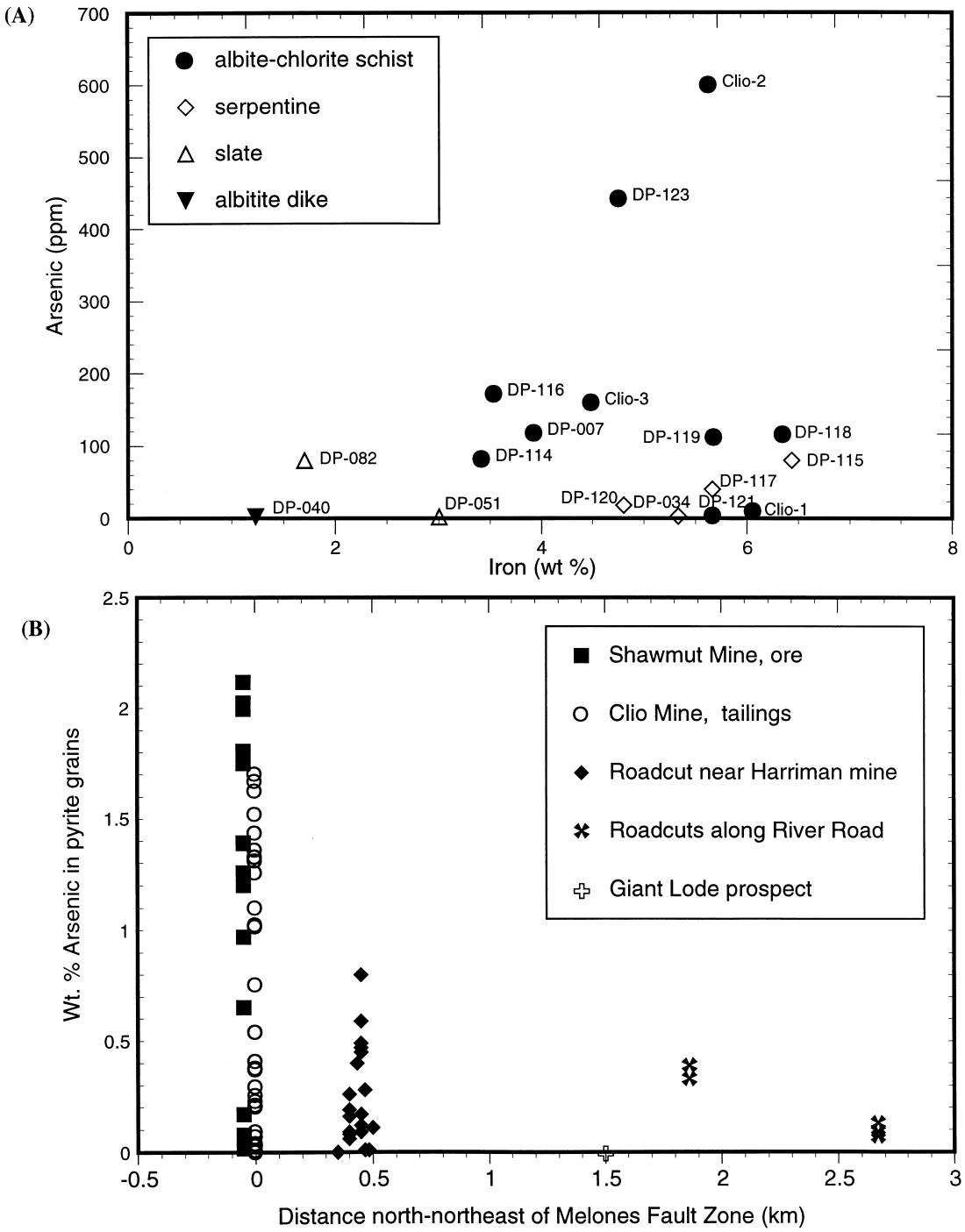

Fig. 2. (A) Arsenic concentration in rocks, outcrops, waste rock and tailings as a function of wt.% Fe. See Table 1 for sample descriptions and locations. (B) Wt% of As in pyrite as a function of distance from the Melones fault zone (MFZ). Zero on the horizontal axis marks the approximate center of the MFZ where samples from the Clio and Shawmut mines are plotted. The distance +0.5 km denotes the eastern edge of the fault zone; the samples here are from a mineralized outcrop in a roadcut (Point X in Fig. 1A). Each data point represents the average of three to nine electron microprobe analyses of a single pyrite grain.

chloritic slates (DP-115, -117, and -120) contain between 18 and 80 ppm As, while albite-chlorite schists have the highest As concentrations, with one sample (Clio-2) containing 600 ppm. With the exception of schist Clio-1 (10 ppm As), seven samples of albite-chlorite schist have As contents between 80 and 600 ppm (Table 2; Fig. 2A).

The albite-chlorite schists in the Clio mine tailings probably originated from the hanging wall ore zone (Knopf, 1929; see Fig. 1B). Sample Clio-2 is a light grey, banded, highly foliated pyrite-bearing albite-chlorite schist. It was collected at an elevation of about 260 m, above the high-water line of Don Pedro Reservoir (maximum level 253 m). This sample contains about 8% pyrite as euhedral crystals ranging from 10 μm to 3 mm in size, with the majority 1–2 mm. Euhedral pyrite crystals typically truncate well developed foliation in the sample, but rotated and deformed crystals are also observed. This suggests prolonged pyrite formation during and after the dynamic metamorphism that produced the schistose texture. Major phases in Clio-2 schist include chlorite and albite. Fine-grained brunsvigite-chlorite is segregated in 1- to 3-mm-thick layers where it is finely intermixed with sericite. Chlorite also occurs as discrete grains up to 3 mm in diameter. Nearly stoichiometric albite occurs as 10–100 μm crystals in aggregates between the chlorite and sericite bands that define the foliation, as well as intergranular aggregates of chlorite. Trace phases include chalcopyrite, Sb-Cu-Fe sulfides, calcite, and quartz. The rock contains numerous veins (100 μm–2 mm wide) of quartz, calcite, ferroan dolomite and titanite. Of the minerals in sample Clio-2, only pyrite contains detectable (by EPMA, see Table 3) concentrations of As.

3.2. Arsenic concentrations in pyrite

Bulk As concentrations were measured in individual pyrite grains from tailings samples at the Clio Mine, from a Shawmut Mine chlorite schist ore sample (sample 8215 from the Stanford University Ore Deposits Collection, collected in 1898; see Fig. 1A), from outcrops of a tectonic melange at the margins of the Melones fault zone (MFZ) (exposed in a roadcut on the Jacksonville Road at point X in Fig. 1A), and from samples collected along the Tuolumne River Canyon NE of the Clio mine. The As concentrations in individual pyrite grains from these samples are shown in Fig. 2B as a function of distance from the MFZ. Average compositions of representative pyrite grains from the Shawmut Mine and from Clio tailings samples are given in Table 3. In sample Clio-2 (600 ppm As in bulk rock; see Fig. 2A), the average As concentration in 13 pyrite grains ranges from <0.01 to 1.63 wt.% (the highest individual analysis is 5 wt.% As and the average for all 13 grains is 1.2 wt.% As). Pyrite grains in sample Clio-1 (10 ppm As in bulk rock) have average As contents between 0 and 0.09 wt.%, and in sample Clio-3 (425 ppm As in bulk rock), average As concentrations in pyrite range from 0.01 to 1.10 wt.%. Arsenic is the most abundant trace element in the analyzed pyrites (Table 3). Up to 0.33 wt.% Pb occurs in the arsenian pyrite grains of sample Clio-2 but Zn, Mn, Sb, Se, Cu, Bi, Co, Ag and Au are all generally much less than 0.1 wt.%. Compositions of pyrite grains in the Shawmut sample are similar to Clio samples, containing between 0.02 and 2.12 wt.% As (Fig. 2B, 14 grains) and up to 0.29 wt.% Pb, with little other trace element content.

The diamond symbols in Fig. 2B represent the average concentrations of As in pyrite grains from outcrops of serpentinite, serpentinized harzburgite, black banded slate, banded carbonates, and albite-chlorite schist from a road cut near the Harriman Mine at the margins of the MFZ (location X, Fig. 1A). Arsenic content of pyrite grains from all these rock types range from <0.01 to 0.8 wt.%. Average compositions of As in pyrite grains from slate of the Calaveras Formation located 1.9 and 2.7 km north of the center of the MFZ (River Road, Fig. 1A) and albite-chlorite schists from a distance of 1.5 km (point Y, Fig. 1A) range from <0.01 to 0.4 wt.% As. The data summarized in Fig. 2 demonstrate that As is concentrated in pyrite grains from mineralized rocks of the MFZ, and that background As concentrations, represented by pyrite grains from the Calaveras Formation north of the MFZ, are <0.5 wt.%.

3.3. Arsenic distribution in pyrite

3.3.1. Electron probe microanalysis

Two grains from sample Clio-2 were selected for detailed chemical analyses by EPMA. Using automated beam motion to analyze a rectangular grid, 7968 analyses were performed throughout Grain 1 with ~20-μm spacing. Excluding four analyses with elemental ratios indicative of arsenopyrite microinclusions, the maximum As concentration in the pyrite was 2.8 wt.%. The mean As concentration was 1.05 wt.%. On Grain 2, 8354 analyses conducted using 10-μm spacing gave a mean As concentration of 1.39 wt.%. Only two analyses were indicative of arsenopyrite composition, with the maximum As concentration in the pyrite 3.9 wt.%. Thus less than 0.05% of these two crystals are arsenopyrite, suggesting that most As is present in solid solution in pyrite, not in microinclusions of separate As phases. Other inclusions in the pyrite grains are elec-

trum (90% Au, 10% Ag) and albite. Both pyrite crystals show similar patterns of As zoning with a core containing less than 1 wt.% As, a zone containing the maximum As concentrations (between 2.8 and 1 wt.% As in Grain 1 and between 3.9 and 1 wt.% in Grain 2), and an outer rim with less than 1 wt.% As. These spatial relationships indicate that the physical and chemical conditions governing As incorporation in the pyrite were not uniform during crystal growth.

3.3.2. High-resolution transmission electron microsopy

Further evidence for As solid solution in Clio-2 pyrite grains, without the formation of separate arsenopyrite phases, comes from HR-TEM structural analysis (Fig. 3). High-resolution imaging shows a distinct absence of marcasite-type structure micro-lamellae in Clio-2 pyrite crystals. If present these structures would suggest subdomains of arsenopyrite, which is isostructural with marcasite (Pósfai and Buseck, 1997).

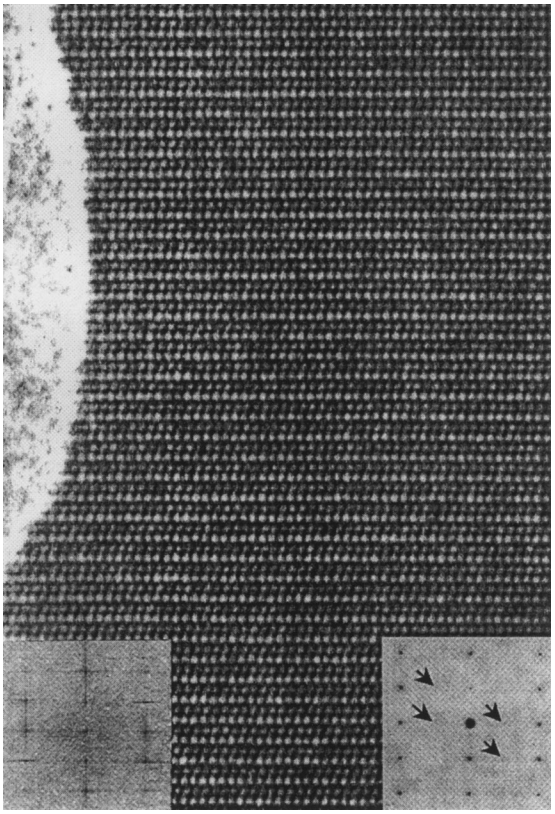

Fig. 3. HR-TEM image ([001] projection) of Clio-2 pyrite showing a lack of stacking faults and defects. Lattice spacing between horizontal layers is 2.7 Å. Left inset: Fourier transform of HR-TEM image. Right inset: selected area electron diffraction (SAED) pattern showing *hk0* reflections with *h* odd reflections (arrows) that are forbidden by the *Pa3* space group of pyrite.

Abundant stacking faults from marcasite lamellae have been observed in pyrite grains in other studies, but these faults do not appear to be directly correlated with As substitution (Dódony et al., 1996; Pósfai and Buseck, 1997). Although the HR-TEM images of Clio-2 pyrite appear perfectly ordered and indicate As solid solution in pyrite, the presence of weak forbidden reflections was observed in selected area electron diffraction (SAED) patterns (arrows on right inset in Fig. 3; see also Pósfai and Buseck (1997)). These reflections are interpreted as a deviation from cubic symmetry caused by shifting single-bonded Fe atoms away from S atoms and double-bonded Fe atoms towards S atoms (Pauling, 1978; Bayliss, 1989). The total As content in the sample is too low to produce the forbidden reflections if it is evenly distributed (Pósfai and Buseck, 1997), but may produce this subtle structural shift if As atoms are clustered within the pyrite structure, which is also supported by results from XAS, discussed next.

3.3.3. X-ray absorption spectroscopy

X-ray absorption spectroscopy was employed to investigate the average local atomic bonding of As in pyrite from the Clio-2 sample. Bulk XAS has the advantage of sampling the average coordination environment around a specific element in a sample, which is useful for determining the most abundant modes of bonding and for overcoming biases from limited sampling by spatially resolved techniques such as TEM. The As X-ray absorption edge position is indicative of its oxidation state. In Fig. 4A, edge positions for Clio-2 pyrite, two weathering product samples (DP 045 and DP 011), and the reference compounds arsenopyrite (FeAsS) and scorodite ($FeAsO_4{\cdot}2H_2O$) are compared. An edge position at higher energy than the absorption edge of elemental As (As^0, represented by the vertical dashed line at 11,867 eV in Fig. 4A), indicates positive oxidation state while an edge position at lower energy indicates a negative oxidation state. Although there are distinct differences in the near-edge shapes of Clio-2 and arsenopyrite spectra, the main absorption edge positions are both shifted to an energy position lower than that of elemental As. Scorodite has an absorption edge higher than that of elemental As and the energy position is similar to that of the weathered samples (Fig. 4A). These edge positions represent differences in As oxidation state (nominally -1 for arsenopyrite; $+5$ for scorodite).

Quantitative fits of EXAFS spectra using theoretical standards calibrated on reference compounds enable the determination of nearest-neighbor atom identities and approximate coordination numbers (to ~5–6 Å from the central atom) and interatomic bond distances

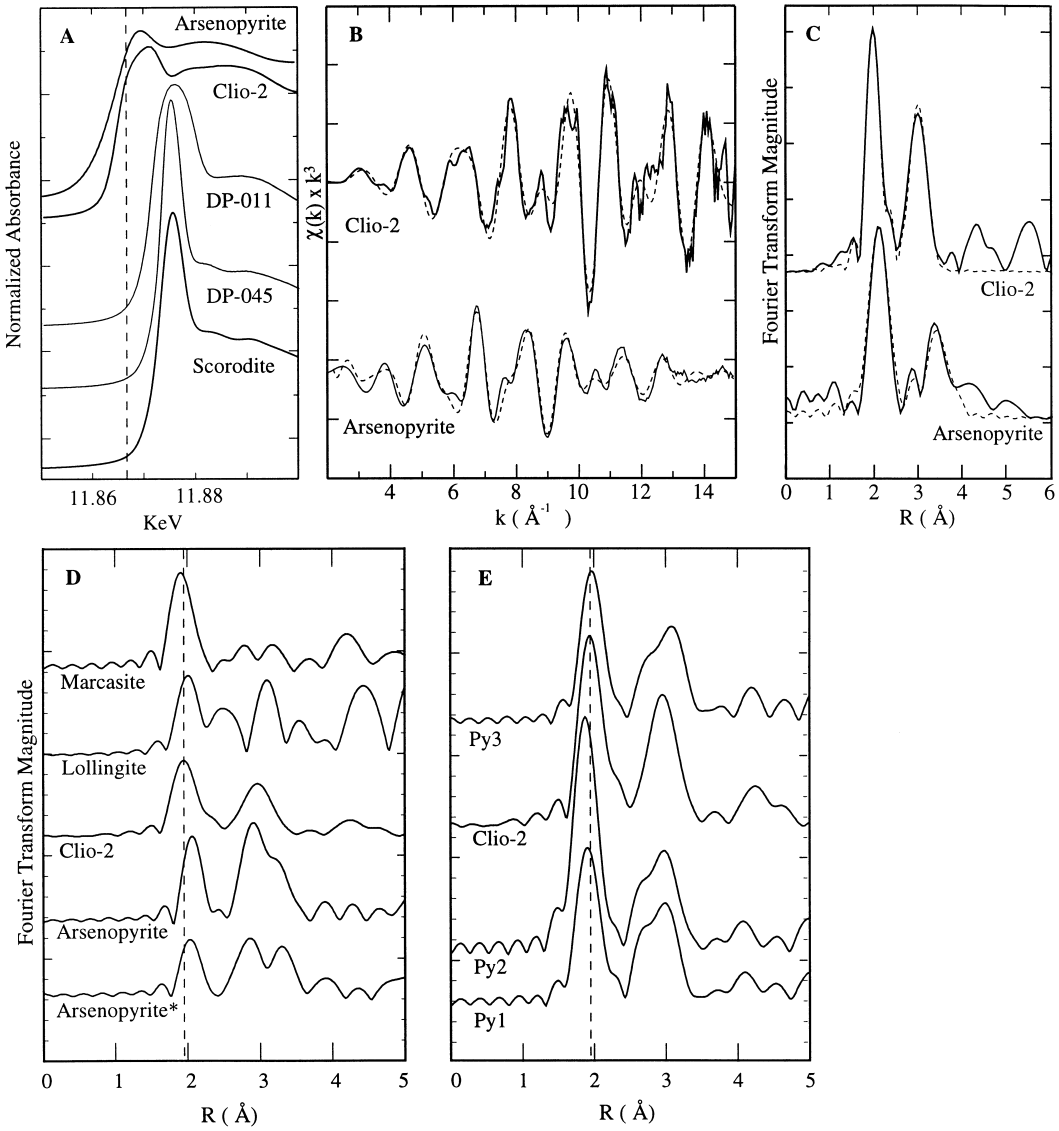

Fig. 4. (A) Arsenic K-edge positions for samples Clio-2, DP-011, DP-045, and reference samples arsenopyrite (FeAsS) and scorodite ($FeAsO_4{\cdot}2H_2O$). The dashed vertical line shows the theoretical absorption edge position for elemental As (11,867 eV). (B) Normalized As-EXAFS spectra and (C) radial structure functions (RSF) for reference arsenopyrite and for sample Clio-2 (collected at cryogenic temperature, about 10 K). Solid line: experimental data; dashed line: least-squares fit using parameters shown in Table 4. Peak positions in RSF do not represent true absorber-backscatterer distances because the RSF are uncorrected for phase-shift effects. Corrected distances (Table 4) are 0.3–0.5 Å longer than RSF peak positions shown. (D) Comparison of Clio-2 RSF with RSF of theoretical EXAFS spectra generated by FEFF (As as central absorber) for arsenopyrite, arsenopyrite* (see text), marcasite with As substituted for S as the central absorber, and löllingite. The second-shell backscattering of theoretical arsenopyrite differs from that of the arsenopyrite data shown in Fig. 4C because all backscatterers were included in the theoretical calculation, including paths (e.g. As–S at 3.09 and 3.18 Å) that were found not to contribute significantly to the experimental EXAFS. (E) Comparison of Clio-2 RSF with (Py1) As substituted for S as the central absorber in pyrite; (Py2) As substituted for S as the central absorber and nearest-neighbor S; and (Py3) as Py1 but with an expanded unit cell (see text). Dashed lines in (D) and (E) show the Clio-2 first shell peak position.

(generally $\pm$ 0.02 Å), as well as an indication of local positional disorder around the central absorber atom (the Debye–Waller factor, σ^2) (e.g., Brown et al., 1988, 1995). For Clio-2 pyrite and arsenopyrite (Fig. 4B and C), EXAFS fits indicate similarities in the local atomic structure around As but clearly show that As in Clio-2 is not bound in arsenopyrite. Fits to spectral features in Clio-2 and reference arsenopyrite differ in first-neighbor backscatterer identities and second-neighbor As–Fe and As–As distances (Table 4). In addition, there are significantly fewer near-neighbor As backscatterers in Clio-2 than in arsenopyrite. Similar first-neighbor As–S distances in Clio-2 and S–S distances in pyrite (Table 4), as well as distance and coordination numbers of near-neighbor Fe atoms, are consistent with the other observations that As substitutes for S in pyrite (FeS_2) as a solid solution. To rule out other modes of As incorporation, the experimental data were compared with theoretical models of EXAFS spectra for As substituted for S in marcasite (a polymorph of pyrite), As in arsenopyrite, As in arsenopyrite with additional As substituted in the first two S shells around a central As atom (arsenopyrite* in Fig. 4D), and As in löllingite ($FeAs_2$).

Table 4
Parameters used in fitting As K-edge EXAFS data for sample Clio-2 and arsenopyrite (see Fig. 4B and C) and interatomic distances in pyrite relative to a central S atom, used to generate models Py1, Py2 and Py3 (see text and Fig. 4E)

Sample	Atom	N	R (Å)	σ^2 (Å^2)
Arsenic K-edge EXAFS fitting parameters[a]				
Clio-2[b]	S	1.0	2.25	0.0021
	Fe	3.0	2.32	0.0018
	S	4.0	3.10	0.0089
	As	3.0	3.17	0.0036
	Fe	4.0	3.50	0.0022
Arsenopyrite[c]	Fe	3.0	2.36	0.0086
	As	1.0	3.06	0.0094
	As	2.0	3.15	0.0152
	As	2.0	3.34	0.0064
	Fe	4.0	3.79	0.0106

Sample	Atom	N	Pyl, Py2 R(Å)	Py3 R(Å)
Interatomic distances from sulfur in pyrite				
Pyrite[d]	S	1.0	2.17	2.23
	Fe	3.0	2.26	2.32
	S	6.0	3.07	3.15
	S	6.0	3.31	3.40
	Fe	3.0	3.44	3.53
	Fe	1.0	3.59	3.69
	Fe	3.0	4.44	4.55
	S	3.0	4.51	4.63
	S	6.0	4.79	4.91
	S	6.0	4.95	5.08
	Fe	3.0	5.14	5.28

[a] N represents the number of backscatters at distance R. σ^2, the Debye–Waller term, is the absorber-backscatterer root-mean-square-displacement of bond length. Errors in the fit analysis based on comparisons of FEFF reference functions to well-known transition metal reference compounds are $R \pm 0.02$ Å and $\sigma^2 \pm 20$–30% (O'Day et al., 1994).

[b] Clio-2 was not fit for atoms more distant than 3.5 Å from the cental absorber. N was held to crystallographic values for pyrite for Fe, but was varied in integer steps for the S and As contributions to achieve the best fit. R and σ^2 were allowed to vary during fitting.

[c] N was held to crystallographic values for arsenopyrite; R and σ^2 were allowed to vary during fitting. Sulfur backscatters at 2.34, 3.09 and 3.18 Å do not contribute significantly to the spectral fit.

[d] In model Py2 (see Fig. 4E), As is substituted for the nearest-neighbor S atom as well as for the central absorber sulfur. Distances used in model Py3 (Fig. 4E) represent a pyrite unit cell expanded by 2.6%.

Comparison of the radial structure functions (RSF) for these phases with the RSF for Clio-2 demonstrates that As in the natural sample is not in the molecular environment represented by any of these phases (Fig. 4D). The Clio-2 RSF has significantly shorter first-shell distances and different second-shell backscattering than the arsenopyrite structures. Compared to löllingite, the first-shell distance in Clio-2 is ~0.2 Å shorter and the second-shell of Clio-2 is broader. The shells present at further distances in löllingite are not present in Clio-2. The marcasite RSF has a first-shell peak position similar to that of Clio-2 and peak positions from 3.4 to 5 Å are also similar, but the second shell of marcasite exhibits a double peak where Clio-2 has only a single peak. There is also considerable disparity in amplitude among all peaks in marcasite and Clio-2. The differences in the RSF rule out the presence of a significant fraction of these phases in the Clio-2 arsenian pyrite sample.

In order to evaluate whether or not As occurs in clusters in pyrite, theoretical EXAFS models were generated for As substitution in one (Py1) and two (Py2) S sites in pyrite (Fig. 4E). In the RSF of As-substituted pyrite, the first-shell peak around As arises from a linear combination of backscattering from one nearest-neighbor S atom (at 2.17 Å) and 3 Fe atoms (at 2.26 Å; see Table 4). Thus, the amplitude of the first-shell peak can be used to estimate the percentage of As in first-neighbor S sites. The Py1 first-shell peak, in which only S is in the first-neighbor S site (As is the central atom), has a smaller amplitude than the Clio-2 first-shell peak. The amplitude of the Py2 first-shell peak, in which only As is in the first-neighbor S site, is greater than that of Clio-2. Interpolation between these two theoretical models indicates ~30% substitution of As for S in nearest-neighbor S sites of Clio-2. Arsenic substitution for S in the second shell around a central As absorber was evaluated by testing the goodness-of-fit using different integer amounts of S and As in the closer S site. The As–S and As–As distances and Debye–Waller factors were allowed to vary independently in this subshell. The best fit (Table 4) was achieved by approximately 43% substitution of As for S in the second-neighbor S site. In the Py1 and Py2 models, coordination numbers and distances for atoms further than 3.2 Å from the central absorber were held constant at the values for pyrite (Table 4).

The Py1 and Py2 models were constructed using the unit cell size of pure pyrite ($a_0 = 5.404$ Å). However, substitution of As into the pyrite structure should increase the unit cell size and the interatomic distances in the neighborhood of As substitution. Least-squares fits of the first shell of the Clio-2 EXAFS spectrum indicate As–Fe distances about 2.6% longer than the S–Fe distances in pure pyrite (Table 4). A third theoretical model (Py3) was calculated using the same As substitution parameters as Py1, but with the pyrite unit cell expanded by 2.6% ($a_0 = 5.544$ Å). This model corrects the mismatch in the first-shell peak between theory and experiment by moving Fe atoms to a longer distance and also shows good agreement for RSF peaks from 4 to 5 Å (Fig. 4E).

Second-neighbor backscatterers for the S position in pyrite are a combination of S and Fe atoms (see Table 4 for pyrite interatomic distances). In all three pyrite simulations, the models predict a distinct shoulder on the second-shell peak at about 2.7 Å in the RSF. This shoulder is mainly due to scattering from S atoms beyond the Fe shell at distances of 3.06 Å and 3.31 Å in pyrite (Table 4). In natural pyrite, disorder attending As substitution for S would tend to smear out these subshell contributions as well as decrease overall peak amplitude. This local disorder was not accounted for in the simulations, but the observations are consistent with previous EXAFS analyses of static disorder in natural compounds (O'Day et al., 1998). Hence, there is good support overall from the model RSF calculations for As substitution for S in pyrite in the Clio-2 sample, with significant clustering of As in the nearest S sites.

3.4. Weathering products: chemistry and mineralogy

Twenty-eight samples of soils, sediments, and weathering crusts were analyzed for bulk As concentration (Table 5; sample numbers and locations in Table 1). Background values, represented by sediments from the Tuolumne River NE of the Melones fault zone (DP-057), and sediments and soils at the reservoir shoreline west of the Clio mine (DP-050, DP-051, DP-053, DP-054, DP-055, and DP-056) are less than 11 ppm. Table 5 also shows the concentrations of Fe, Cr, Ni, Mn and Zn, and identifies the major secondary phases in representative samples. The unusually high values of Cr and Ni in some samples (e.g. DP-001 and DP-113) reflect the ultramafic protolith of many of the weathering products.

The highest concentrations of As are found in weathering products of tailings at the Clio mine and of the fault melange at point X in Fig. 1A. Weathering products at the Clio mine are reddish-brown, fine-grained crusts on rocks, vegetation, mine foundations, and machinery. They are primarily goethite (Table 5) and contain up to 1260 ppm As (sample DP-011). Shoreline reservoir sediments at the Clio mine (DP-TNT, Table 5) contain 30 ppm As, a concentration 3 to 10 times greater than in reservoir sediments west of the mine (Table 5). Weathering products of the Melones Fault melange at point X in Fig. 1A consist primarily of SO_4 salts including jarosite and gypsum with

Table 5
Concentrations of Fe, As, Cr, Ni, Mn and Zn in sediments and fine-grained weathering products[a]

Sample[b]	Fe, %	As, ppm	Cr, ppm	Ni, ppm	Mn, ppm	Zn, ppm	WM[c]
Clio mine tailings pile							
DP-TNT[X]	7.86	30	550	204	840	65	
DP-011[Y]	11.85	1260	540	148	245	270	goe, gyp
DP-011[Y]	12.85	1625	487	147	260		goe, gyp
DP-111[Y]	10.80	1	264	109	605	22	
DP-112[Y]	13.55	620	693	238	570	94	goe
DP-113[Y]	4.56	16	906	200	710	62	
DP-122[Y]	13.20	1	349	155	655	22	goe
DP-124[Y]	8.60	2	822	182	785	42	
Melones fault zone melange (Point X in Fig. 1A)							
DP-001[Y]	17.10	1300	1015	109	280	174	jar, gyp
DP-001[Y]	> 25.0	2150	2380	122	290		jar, gyp
DP-025[X]	5.37	103	146	66	1100	112	
DP-030[X]	7.16	234	802	635	760	118	jar
DP-043[X]	3.36	< 3	1130	883	668	66	
DP-044[X]	5.75	140	813	654	1520	201	
DP-045[Y]	8.47	1025	555	126	280	102	jar, gyp
DP-045[Y]	17.20	1790	833	118	230		jar, gyp
DP-046[X]	4.03	28	892	725	777	68	
DP-047[Y]	7.80	395	823	189	460	172	jar
DP-047[Y]	11.45	775	1130	214	420		jar
DP-067[X]	3.63	50	167	46	955	125	
DP-074[Y]	16.25	1000	235	66	795	186	jar, cal
DP-075[X]	4.54	185	261	15	105	28	jar, gyp
DP-080[X]	4.42	45	1150	840	703	57	
DP-081[X]	1.72	48	566	327	239	37	
Don Pedro Reservoir shoreline sediments west of Clio Mine[d]							
DP-050[X]	7.24	5	302	129	2080	142	hem
DP-052[X]	4.51	< 3	123	28	790	71	
DP-053[X]	5.35	4	125	46	1610	138	
DP-054[X]	4.43	6	229	44	1210	142	
DP-055[X]	5.28	11	158	57	772	112	
DP-056[X]	5.28	< 3	198	50	1550	131	
D. Outside fault zone[e]							
DP-038[X]	6.11	67	110	33	850	58	hem, goe
DP-057[X]	5.20	< 3	488	63	728	218	

[a] See Table 1 for sample descriptions. Bold sample numbers denote analyses of < 63-μm size fraction. All other analyses are for bulk samples.

[b] Chemical analysis of samples denoted with superscript X was conducted at XRAL Laboratories (Don Mills, Ontario, Canada); analysis of samples denoted with superscript Y was conducted at Chemex Laboratories, Sparks, NV. All analyses by ICP-AES. Splits of weathering product samples DP-001, -011, -045, and -047 were dry-sieved using non-metallic screens to separate the < 63-μm fraction for chemical analysis (bold).

[c] Mineralogy of weathering products in sample, excluding detrital minerals; goe, goethite; jar, jarosite; gyp, gypsum; hem, hematite; cal, calcite. X-ray diffraction was conducted on a Rigaku CN 2029 diffractometer with Cu Kα radiation. Mineralogical identifications were made by comparison with JCPDS reference files.

[d] Samples DP-050, -052, -053, -054, -055, -056 located approximately 0.5 km WNW of the Clio Mine. Sample DP-067 located 0.2 km SSW (along strike) of point X in Fig. 1A.

[e] Sample DP-038 located at point Y in Fig. 1A. Sample DP-057 located at the Ward's Ferry Bridge, approximately 2 km NE of map area shown in Fig. 1A.

As concentrations up to 1300 ppm (Table 5). The concentration of As in the weathering products is highly variable, ranging from background levels (i.e., <11 ppm) to values exceeding 1000 ppm. This variability reflects the heterogeneous distribution of As in outcrops and tailings (Fig. 2) and the mobility and mixing of friable fine-grained weathering products with As-poor detrital minerals by wind and rain runoff during storm events.

The concentration of As in sediments, soils, and weathering products (Table 5) is shown in Fig. 5 as a function of total Fe content. For comparison, whole rock As concentrations (Table 2) are also shown (solid circles). As is concentrated in weathering products relative to whole rocks, and the concentration of As in the weathering products increases with increasing total Fe content (Fig. 5). The latter observation reflects the efficiency of As sorption on and coprecipitation with Fe-oxides, -hydroxides, and -sulfates. The thin crosses in Fig. 5 for samples DP-001, DP-011, DP-045, and DP-047 represent As and Fe concentrations in the <63-μm fraction of these samples (Tables 5 and 6). Arsenic is concentrated in the smaller size fractions, increasing, for example, from 1300 ppm in the bulk sample of DP-001 to 2150 ppm in the <63-μm fraction (Fig. 5, Table 6).

Two samples representative of high-As weathering products near the Clio mine (DP-011 and DP-045) were chosen for examination of grain size, chemistry, mineralogy, and atomic environment of As. Table 6 shows the chemical composition of the bulk samples and the <63 μm size fraction of each sample. Sample DP-011 is a rust-colored, Fe-rich weathering crust collected from an outcrop of chlorite schist (Mariposa Formation) at the base of a prominent concrete foundation at the Clio mine, above the high water level of Don Pedro Reservoir. Composed of a very fine-grained, friable mixture of goethite, quartz, albite and chlorite, this sample is typical of the weathering products found near the Clio mine site. Sample DP-045 is a weathering crust composed of jarosite, albite and saponite, collected from an outcrop composed of talc, albite and pyrite. This outcrop, in the roadcut at point X in Fig. 1A, has been exposed to atmospheric weathering since 1970. Extensive oxidative dissolution of pyrite near its surface is evident by abundant cubic

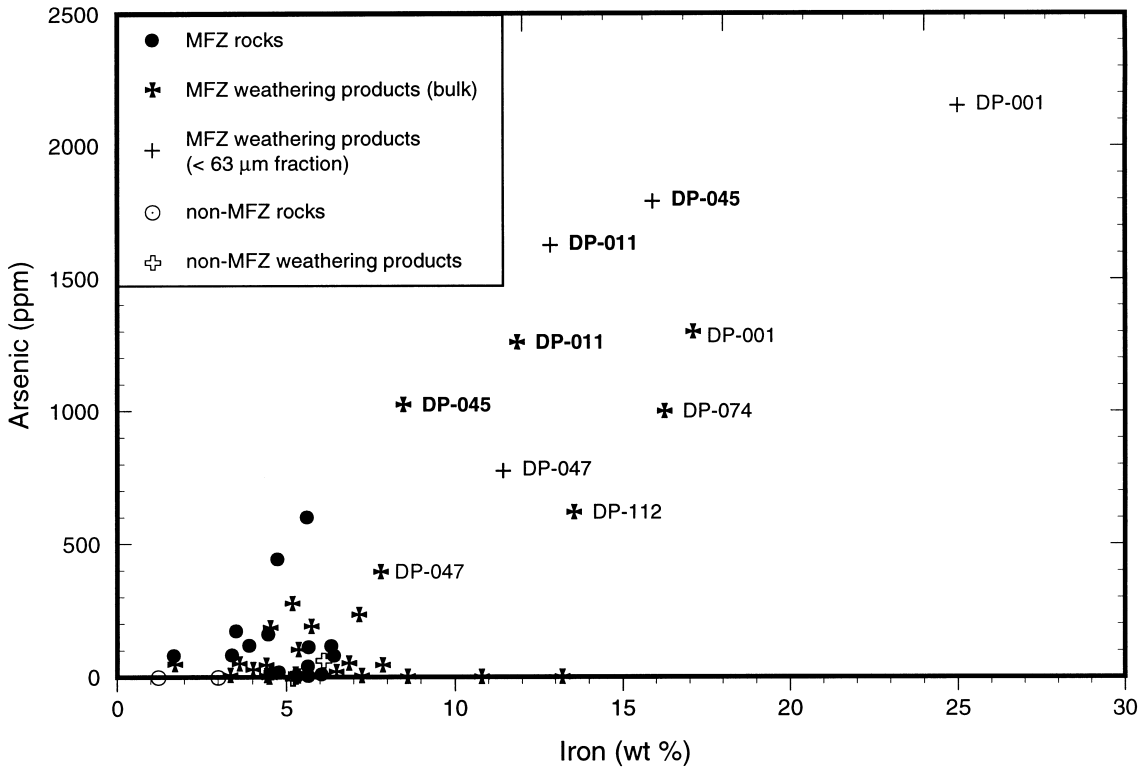

Fig. 5. Arsenic concentration in rocks and weathering products (sediments, soils and crusts) as a function of weight-percent Fe and location relative to the Melones Fault Zone (MFZ). See Table 1 for sample descriptions and locations, and Tables 5 and 6 for chemical analyses.

pores. Unit cell dimensions for jarosite in the sample (calculated from 13 XRD peak positions) are $a = 7.31 \pm 0.01$ Å and $c = 17.14 \pm 0.026$ Å, values consistent with those reported and summarized by Alpers et al. (1992) for K-jarosite. Energy-dispersive X-ray analysis combined with SEM imagery indicates that the jarosite occurs as very small attached particles or coatings on other minerals in the sample. For these two surficial samples, both the As and Fe X-ray absorption edges and EXAFS were examined to characterize the oxidation state and coordination of As in the host Fe minerals (goethite and jarosite).

3.5. Arsenic in goethite-rich weathering crusts

Fig. 6A and B compares the Fe K-edge EXAFS spectra and RSF of sample DP-011 (< 63-μm fraction) and synthetic goethite. Fit results for DP-011 and synthetic goethite converge on the same values for interatomic distances (within error) for all shells (Table 7), consistent with XRD results indicating that goethite is the predominant Fe phase in sample DP-011. Differences between the two spectra (e.g., peak height and broadness for peaks between ~2.5 and 3.8 Å, RSF of Fig. 6B) arise from variations in amplitude among overlapping shells of second-neighbor Fe atoms. The EXAFS interatomic distances for two of the three Fe–Fe shells in DP-011 and synthetic goethite are contracted relative to crystalline goethite distances calculated from XRD (Szytula et al., 1968; Table 7). In addition, values for the Debye–Waller factor (σ^2) are increased for these two Fe shells relative to the closer Fe–Fe shell at 3.03 Å. The contraction in interatomic distances, the increased disorder, and the differences in amplitude between the natural and synthetic samples probably result from local atomic disorder around Fe arising from small domains of non-goethite Fe oxyhydroxide, chemical impurities, or small particle size (O'Day et al., 1994). Previous characterization of the synthetic goethite sample indicated only crystalline goethite and no evidence for other Fe oxyhydroxide

Table 6
Surface area, mean particle size, and chemical analyses of weathering product samples used for EXAFS analysis[a]

Surface area, $m^2\ g^{-1}$; mean particle size, μm	DP 011	**DP 011** 40; 0.1	DP 045	**DP 045** 12; 36
Al_2O_3, %	10.64	10.38	7.74	na
CaO, %	2.11	1.78	0.68	na
Cr_2O_3, %	0.13	0.11	0.12	na
Fe_2O_3, %	21.72	23.73	14.95	na
K_2O, %	0.44	0.45	0.97	na
MgO, %	5.09	5.25	10.73	na
MnO, %	0.05	0.05	0.05	na
Na_2O, %	2.17	2.09	3.65	na
P_2O_5, %	0.09	0.08	0.42	na
SiO_2, %	47.93	47.92	48.24	na
TiO_2, %	0.56	0.48	0.46	na
LOI, %	8.41	6.87	10.80	na
Total, %	99.34	99.19	98.81	na
V, ppm	131	130	361	566
Cr, ppm	540	487	555	833
Mn, ppm	245	260	280	230
Fe, %	11.85	12.85	8.47	17.20
Co, ppm	17	25	11	15
Ni, ppm	148	147	126	118
Cu, ppm	121	128	54	100
Zn, ppm	270	338	102	102
As, ppm	1260	1625	1025	1790
Sr, ppm	63	68	186	449
Mo, ppm	6	5	2	6
Ba, ppm	120	100	90	130
Pb, ppm	52	60	4	22

[a] Bold sample numbers denote < 63-μm size fraction. Analyses performed at Chemex Laboratories, Sparks, NV. Major elements (upper portion of table) by XRF. Arsenic by hydride-generation atomic absorption spectroscopy (AAS). Lead by AAS. Iron and other trace elements by ICP-AES.

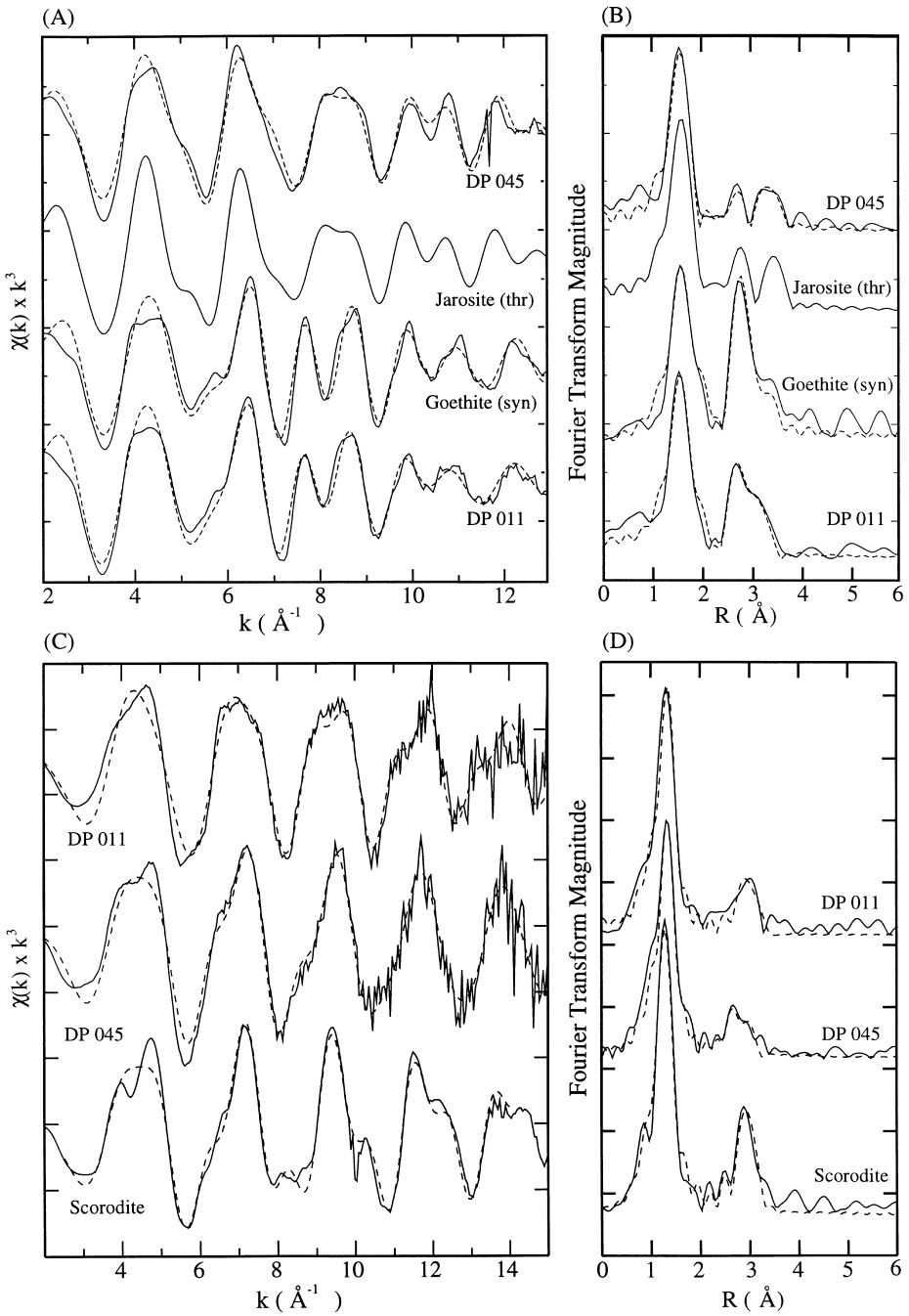

Fig. 6. (A) Normalized Fe K-edge EXAFS spectra and (B) radial structure functions (RSF) for samples DP-011, DP-045, synthetic goethite and a theoretical model spectrum of jarosite using crystallographic distances from XRD and Debye–Waller factors similar to those obtained during fitting of sample DP-045 (see Table 7). (C) Normalized As K-edge EXAFS spectra and (D) RSF for samples DP 011 and DP-045 compared with reference spectra for scorodite ($FeAsO_4{\cdot}2H_2O$). Solid line: experimental data; dashed line: least-squares fit using parameters shown in Table 7. Sample DP 045 is fit with arsenate substituting for SO_4 in the jarosite structure (see text). Arsenic spectra of DP–011 and DP-045 were collected at cryogenic temperature (~10 K); spectra of goethite and scorodite were collected at room temperature. RSF are shown uncorrected for backscatterer phase shifts.

Table 7
Parameters used in fitting EXAFS data for weathering products and related model compounds[a]

	Atom	N	R(Å)	σ^2(Å^{-1})
Iron K-edge EXAFS fitting parameters				
DP 011[b]	O	3.0	1.97	0.0046
	O	2.9	2.11	0.0080
	Fe	2.1	3.03	0.0065
	Fe	2.3	3.19	0.0137
	Fe	4.1	3.41	0.0118
Goethite (syn)[c]	O	3.0	1.97	0.0042
	O	3.0	2.11	0.0068
	Fe	2.0	3.03	0.0039
	Fe	2.0	3.19	0.0145
	Fe	4.0	3.42	0.0096
DP 045[b]	O	4.8	1.97	0.0052
	S	2.2	3.23	0.0056
	K	1.7	3.44	0.0073
	Fe	3.0	3.63	0.0075
Crystallographic interatomic distances[e]				
Goethite (xl)	O	2.0	1.953	
	O	1.0	1.954	
	O	2.0	2.089	
	O	1.0	2.093	
	Fe	2.0	3.010	
	Fe	2.0	3.281	
	Fe	4.0	3.459	
Jarosite (xl)	O	4.0	1.983	
	O	2.0	2.062	
	S	2.0	3.227	
	K	2.0	3.564	
	Fe	4.0	3.658	
Arsenic K-edge EXAFS fitting parameters				
DP 011[b]	O	4.3	1.70	0.0025
	Fe	1.7	3.23	0.0039
	Fe	1.1	3.47	0.0051
DP 045[b]	O	4.2	1.70	0.0014
	Fe	1.8	3.32	0.0065
	K	1.3	3.04	0.0077
Scorodite[d]	O	4.3	1.68	0.0022
	Fe	4.0	3.36	0.0025

[a] N represents the number of backscatters at distance R. σ^2, the Debye–Waller term, is the absorber-backscatterer root-mean-square-displacement of bond length. Errors in the fit analysis based on comparisons of FEFF reference functions to well-known transition metal reference compounds are $R \pm 0.02$ Å and $\sigma^2 \pm 20$–30% (O'Day et al., 1994).

[b] N, R and σ^2 were varied independently during fitting. Iron K-edge spectra were collected at room temperature; As K-edge spectra were collected at cryogenic temperature (~10 K).

[c] Synthetic goethite synthesized by Bargar using method of Van Geen et al. (1994). N was fixed to crystallographic values; R and σ^2 were varied independently. Two of the four Fe–O distances in crystalline goethite cannot be resolved within EXAFS fitting error ($R = \pm 0.02$ Å). First-shell distances were grouped into two Fe–O shells (N = 3 for each) for least-squares fits of the EXAFS spectra for the synthetic goethite sample. Three Fe–Fe shells were used to fit the spectrum from 3.0 to 3.5 Å based on crystallographic distances for goethite.

[d] Scorodite fitting parameters from Foster et al. (1998).

[e] Interatomic distances represented as distance from a central Fe atom. Jarosite calculated from XRD data reported by Menchetti and Sabelli (1976); geothite calculated from neutron diffraction data by Szytula et al. (1968).

phases (Van Geen et al., 1994; Bargar, personal communication). The disorder seen with EXAFS is therefore on the local atomic scale and may be related to small particle size (< 1 μm by SEM for synthetic goethite, and mean 0.1 μm for sample DP-011, Table 6) but is not due to the presence of significant amounts (> 5%) of another Fe phase.

Comparison of the As K-edge of DP-011 with the reference compound scorodite shows a coincidence of absorbance maxima and edge positions (Fig. 4A), clearly indicating the presence of only As(V) and no As(III) in the natural sample. Analysis of the As K-edge EXAFS of DP-011 (Fig. 6C) indicates As(V) in tetrahedral coordination with O and second-neighbor Fe atoms. Fit discrepancies in the first oscillation of the EXAFS spectrum for DP-011 (at about 4.4 $Å^{-1}$ in Fig. 6B) are similar to those in the scorodite model compound. Previous study shows that these features are associated with multiple scattering among As and O in tetrahedral coordination (Foster et al., 1998). Second-neighbor As–Fe EXAFS distances in sample DP-011 (Table 7) are consistent with bidentate corner-shar-

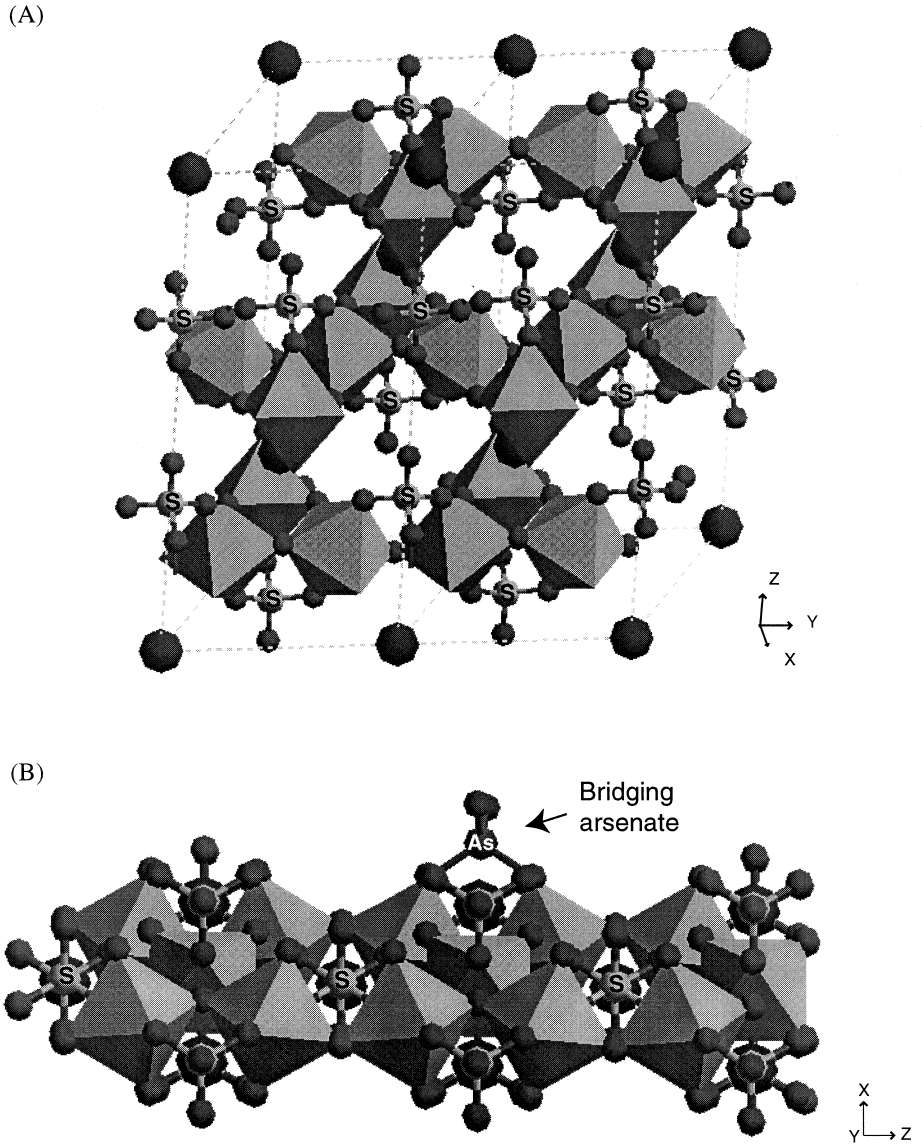

Fig. 7. (A) Molecular model of jarosite showing Fe octahedra (shaded), sulfur (S), K (large spheres) and O (small dark spheres) of two unit cells. (B) Potential sorption site for arsenate bridging two Fe octahedra on the (100) surface of jarosite. For clarity, not all O atoms are shown.

ing of As tetrahedra and Fe octahedra. There is no evidence for a separate scorodite phase. The best fit for the DP-011 spectrum shows two As–Fe shells at 3.23 and 3.47 Å (Table 7). These distances are similar, but not identical, to those found for laboratory samples of As sorbed to ferrihydrite, goethite (α-FeOOH), and akaganeite (β-FeOOH) reported by Waychunas et al. (1993, 1996) and Foster et al. (1998). The present Fe–As distances are 0.07 and 0.18 Å shorter than the two As–Fe shells reported by Waychunas et al. (1993) for arsenate sorbed on crystalline goethite, but are closer (0.07 and 0.03 Å shorter) to those reported by Foster et al. (1998).

3.6. Arsenic in jarosite-rich weathering crusts

Iron in jarosite is octahedrally coordinated with O, as it is in goethite. The spectral features of Fe K-edge EXAFS of sample DP-045 are similar to the jarosite spectrum (Fig. 6A) calculated from the jarosite crystal structure (Fig. 7A). In EXAFS fits, the two Fe–O distances expected in the Fe octahedral site of crystalline jarosite (Table 7B) could not be resolved in sample DP-045 and one Fe–O distance (1.97 Å) was used. The third-shell Fe–K and Fe–Fe distances are similar and produce a broad peak in the RSF at about 3.4 Å (Fig. 6B). The shape of this peak is very sensitive to small changes in Fe–Fe and Fe–K distances and to σ^2 values for each shell because of their similar distances from the Fe central absorber. The central Fe–K distance is slightly decreased in sample DP-045 (3.44 Å) relative to crystalline jarosite (3.56 Å). Such discrepancies in fit may be the result of small quantities of other Fe-bearing minerals in the sample.

The As K-edge EXAFS of sample DP-045 (Fig. 6C) indicates arsenate tetrahedra associated with Fe. The absorption edge position compared with scorodite (Fig. 4A) demonstrates that all of the As is As(V). Fitted As–Fe distances in sample DP-045 (3.32 Å) are slightly longer than the S–Fe distances in jarosite (3.23 Å; Menchetti and Sabelli 1976). The 0.09 Å difference in distance is attributed to the larger size of As relative to S, which would locally distort the jarosite structure around As. The EXAFS data is consistent with most of the arsenate in the sample substituting for SO_4 in jarosite. It is also possible that some arsenate is adsorbed to jarosite rather than substituting structurally (see the following and Fig. 7B), or associated with small domains of other Fe-bearing minerals such as goethite. If these were the dominant modes of sorption, the authors would expect reduction in interatomic As–Fe coordination numbers as a result of bonding on the surface and shifts in interatomic distances. Substitution of arsenate for sulfate in synthetic samples was reported by Dutrizac and Jambor (1987) and Dutrizac et al., (1987), and in natural jarosite-bearing samples by Scott (1987), Huggins et al., (1997) and Foster et al., (1998). The possibilities for compensating the charge imbalance attending such substitution are addressed below in the discussion of As distribution in secondary phases.

4. Discussion

4.1. Arsenian pyrite in source rocks

Arsenic is elevated in albite-chlorite schists and other rocks of the Melones fault zone (MFZ) in which arsenian pyrite comprises up to 15% of ore samples. The results from XAS, electron microprobe, and TEM analyses of arsenian pyrite in sample Clio-2, a high-As albite-chlorite schist of the Clio Mine, provide three independent lines of evidence that As is present as a solid solution within pyrite and not as micro-inclusions of arsenopyrite or other As-bearing phases. The extent to which As distribution within this solid solution is heterogeneous can influence pyrite reactivity in the weathering environment.

Theoretical spectra compared to experimental EXAFS data suggests that there is clustering of the As in the Clio-2 pyrite, with ~30% of first neighbor S sites and ~43% of second neighbor S sites replaced with As, giving a mean cluster composition of ~36.5% As. This composition is consistent with either large homogeneous clusters occupying about 3% of the pyrite volume (assuming all As residing randomly in clusters of composition $FeAs_{0.73}S_{1.27}$, the formula resulting from 36.5% replacement of S with As) or with domains of FeAsS composition, but not with pure $FeAs_2$ clusters. Homogenous clusters could have any size provided they are large enough that interface sites between cluster and bulk are a small fraction of the total contribution to the EXAFS, which sums the signal from all As sites. This type of clustering would not be visible in TEM images or electron-diffraction patterns (Pósfai and Buseck, 1997), and is thus consistent with the present observations.

Domains of FeAsS composition consistent with the present results could assume either of two end-member geometries: clusters of ~27 pyrite unit cells (assuming bulk composition of 50% As in a cluster and 25% arsenic at the cluster/bulk interface), or single layers one unit cell thick. A mineralizing fluid high in As could produce monolayers of FeAsS composition but pyrite structure during pyrite growth if arsenopyrite is unable to nucleate on the pyrite surface. Local strain energy associated with a distorted pyrite layer high in As may prohibit formation of a second high-As layer. Pyrite monolayers of FeAsS composition could also be produced during cooling of a metastable solid solution.

Clark (1960) deduced from phase-equilibria studies that the maximum equilibrium solubility of As in pyrite is ~0.53 wt.% at 600°C, less than half the average concentration (1.2 wt.%) in pyrite from sample Clio-2. Exsolution may or may not lead to formation of a discrete arsenopyrite phase depending on lattice strain energy, temperature, and diffusivities.

Elevated concentrations of As are not generally associated with heavily defective regions in pyrite by TEM (Pósfai and Buseck, 1997), but the high As content might create lattice strain that could produce a defect without close spatial association between As monolayers and the defect. Defects associated with layers of an "arsenopyrite-like" structure might produce faults such as those observed on {001} planes of arsenian pyrite by Fleet et al. (1989). Dódony et al. (1996) also observed planar defect faults, but found them oriented perpendicular to one of the [001] axes in individual crystals. The TEM results do not appear to support the monolayer cluster model since defect faults are not observed, implying larger clusters with lower average As content. However, single layers of pyrite with composition FeAsS may not generate sufficient deformation or contrast to be readily discernable in TEM lattice images.

Weathering textures suggest that arsenian pyrite from the Clio mine is more reactive than pyrite without As. Similar observations have been made for arsenian pyrite samples from coals (e.g., Huffman et al., 1994). Fleet et al. (1993) also found that the As-rich zones of oscillatory-zoned arsenian pyrite were preferentially leached by $KMnO_4$ relative to As-poor zones. Arsenic replacing S in pyrite creates p-type semiconducting regions that trap electrons (Moller and Kersten, 1994), causing increased electrical and ionic conductivity of the pyrite (Evangelou and Zhang, 1995). A consequence of the p-character is a difference between the electrochemical potential of an arsenian pyrite region and other sulfides, such as pure pyrite or n-type pyrite. Contact with aqueous electrolyte solutions thus leads to a conducting cell, which can foster an enhanced dissolution rate of arsenian pyrite (Evangelou and Zhang, 1995).

The type of As cluster in pyrite and its effect on p-character has important consequences for pyrite reactivity. Layers of FeAsS in the pyrite structure may have enhanced p-character over domains with less As. However, such small reactive regions are likely to be electronically mitigated by the surrounding pyrite matrix so that dissolution is not greatly enhanced. In contrast, large domains of high-As pyrite at the grain surface surrounded by low As pyrite may be preferentially dissolved, leading to an increase in porosity and surface area of the remaining pyrite and thus to overall enhanced dissolution. Pyrite at the Clio mine is zoned with low As concentrations at the grain perimeters. However, interior high-As zones are exposed to weathering in crushed tailings material, and in outcrop surfaces and fracture zones, leading to increased reactivity in the weathering environment and to the production of secondary phases which facilitate the transport of As into aquatic environments.

4.2. Arsenic distribution in secondary phases

Arsenic released to the aqueous environment by the weathering of arsenian pyrite may remain dissolved, adsorb onto secondary phases and colloids, or coprecipitate with secondary phases. Samples described in this study provide natural examples of the second two processes. Conditions governing As uptake are related to pH, redox conditions, and available substrate minerals. Fig. 8 illustrates stability fields for selected Fe

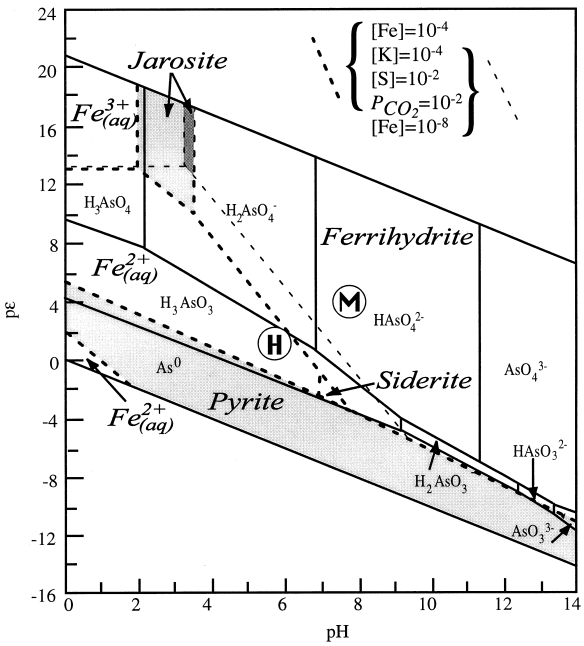

Fig. 8. Superimposed predominance diagrams for the Fe–S–K–CO_2–H_2–O_2 system (after Nordstrom and Munoz (1994)), and for the As–H_2–O_2 system as a function of pH and pε at 25°C, 1 bar. Arsenic speciation (solid phases not shown) from thermodynamic data in Bowell (1994), Cherry et al. (1979), Pokrovsky et al. (1996) and Hem (1977). Arsenic predominance fields denoted by light solid lines, small type; Fe stability and predominance fields denoted by dashed lines, large italic type. Dark dashes denote Fe concentration 10^{-4} M; light dashes for Fe concentration 10^{-8} M. Pyrite and jarosite fields shaded. Darker shading in jarosite field reflects the lower (10^{-8} M) Fe concentration. Approximate pε and pH of lake waters from the Don Pedro Reservoir winter mixis and summer hypolimnion are shown as Points M and H, respectively.

minerals and predominance fields for aqueous Fe species in the system Fe–S–K–CO_2–H_2–O_2; predominance fields for aqueous As species are superimposed on the Fe diagram. Both ferrihydrite, a precursor to goethite (Schwertmann and Fischer, 1973; Schwertmann et al., 1985), and jarosite are common weathering products of pyrite. Ferrihydrite precipitates under pH-neutral, oxidizing conditions, whereas jarosite is stable only under acidic oxidizing conditions and requires a source of K. In the vicinity of the Clio mine, goethite is abundant as a weathering crust associated with heterogeneous waste rock piles where acid produced during pyrite oxidation is readily neutralized by weathering of carbonate minerals. Jarosite is localized on near-vertical outcrops of pyritic talc-albite rocks and is spatially separated from carbonate-bearing rocks with higher acid neutralization potential. Under the oxidizing conditions that promote the formation of both jarosite and ferrihydrite/geothite, aqueous arsenate [As(V)] species rather than arsenite [As(III)] predominate (Fig. 8).

The capacity of secondary minerals to incorporate As influences its mobility in diverse environments, including mine waste and waters with which it reacts. Weathering crusts in the mine environment contain multiple phases, but only a subset of these phases control As mobility by sorption or coprecipitation uptake. Modal mineralogy, surface area, As concentrations, and molecular geometries from EXAFS analysis, in conjunction with sorption site density analyses from model systems, can be used to estimate maximum sorption capacity for As in complex natural samples such as those from the Clio mine area. In sample DP-011, goethite comprises approximately 30 mole % of the <63 μm fraction and the surface area of this size fraction is approximately 40 m^2/g (Table 6). If it is assumed that all minerals in the sample have the same surface area per mole (a conservative estimate, since the goethite is probably much finer-grained than other minerals in this size fraction of the sample, such as quartz), the surface area attributed to goethite is 12 m^2/g sample. Estimates of site density for bidentate inner-sphere sorption on goethite vary from 0.8 sites/nm^2 (for phosphate; Hansmann and Anderson, 1985) to 4.3 sites/nm^2 (number of surface O atoms on (010) surface, divided by two; Koretsky et al., 1998). If a value intermediate in this range, 2 sites/nm^2, is assumed and all As in the sample (1625 μg/g) is surface sorbed in bidentate fashion, then ~54% of the goethite surface sites would be occupied by arsenate. Although there is considerable uncertainty in the actual site density of As on goethite, this calculation suggests that sorption capacity has not been reached in this sample and thus, it could still act as a mineralogic sink for As.

A similar calculation for sample DP-045, in which jarosite is the predominant Fe mineral, shows that As cannot be accomodated only by adsorption on jarosite and confirms the conclusion from EXAFS that substitution for SO_4 in the mineral structure is the dominant mode of arsenate association. Substitution could occur at SO_4 structural sites within the mineral or at the surface termination of the bulk structure. Potential sorption sites are exposed on the (100) surface of ideal jarosite (Fig. 7B). The surface area of DP-045 (<63-μm fraction) is approximately 12 m^2/g (Table 6). Jarosite comprises ~50% of the sample, providing a surface area of 6 m^2/g assuming surface area proportional to molar modal abundance. For a sorption site density of 0.67 sites/nm^2 (calculated for the surface site shown in Fig. 7B) and occupation of all sorption sites on jarosite by As, about 500 μg/g As could be accommodated. This is only ~30% of the 1790 μg/g As present in the sample and suggests that, at a minimum, 70% of the As must be incorporated by substitution within the bulk mineral. Extensive substitution of SO_4 by arsenate occurs in alunite-jarosite group minerals that include coupled charge balancing subsititutions, especially those involving Pb (Scott, 1987; Rattray et al, 1996). Experimental work on simple synthetic systems is needed to quantify the maximum arsenate substitution and sorption capacities of jarosite and other Fe–SO_4 minerals.

4.3. Predictions for arsenic mobility at Don Pedro Reservoir

The mobility and bioavailability of As in mine tailings and their weathering products is governed by its geochemical environment. Mobilization of As from the Clio Mine tailings pile and nearby outcrops begins with oxidation of arsenian pyrite and the formation of friable weathering crusts. Disaggregation and washoff of these crusts by wind, rainfall/runoff and shoreline wave action during winter storm events cause As-bearing secondary minerals (goethite, jarosite) to be transported into Don Pedro Reservoir. Intense wake-waves generated by recreational speedboats contribute to shoreline erosion during the summer months, when rainfall is infrequent in this part of California.

Once introduced to the lake environment (Fig. 9A), As partitioning between solid and aqueous phases is affected by stratification and turnover (e.g., Aggett and O'Brien, 1985; Seyler and Martin, 1989; Belzile and Tessier, 1990; De Vitre et al., 1991; Kuhn and Sigg, 1993), and by variations in pH and redox potential (Cherry et al., 1979; Thanabalasingam and Pickering, 1986). During the winter mixis, monomictic Don Pedro Reservoir is well mixed and oxygenated, with a pH near neutral (Point M in Fig. 8). Under these conditions, goethite transported into the reservoir is stable, but some of the associated arsenate is expected to des-

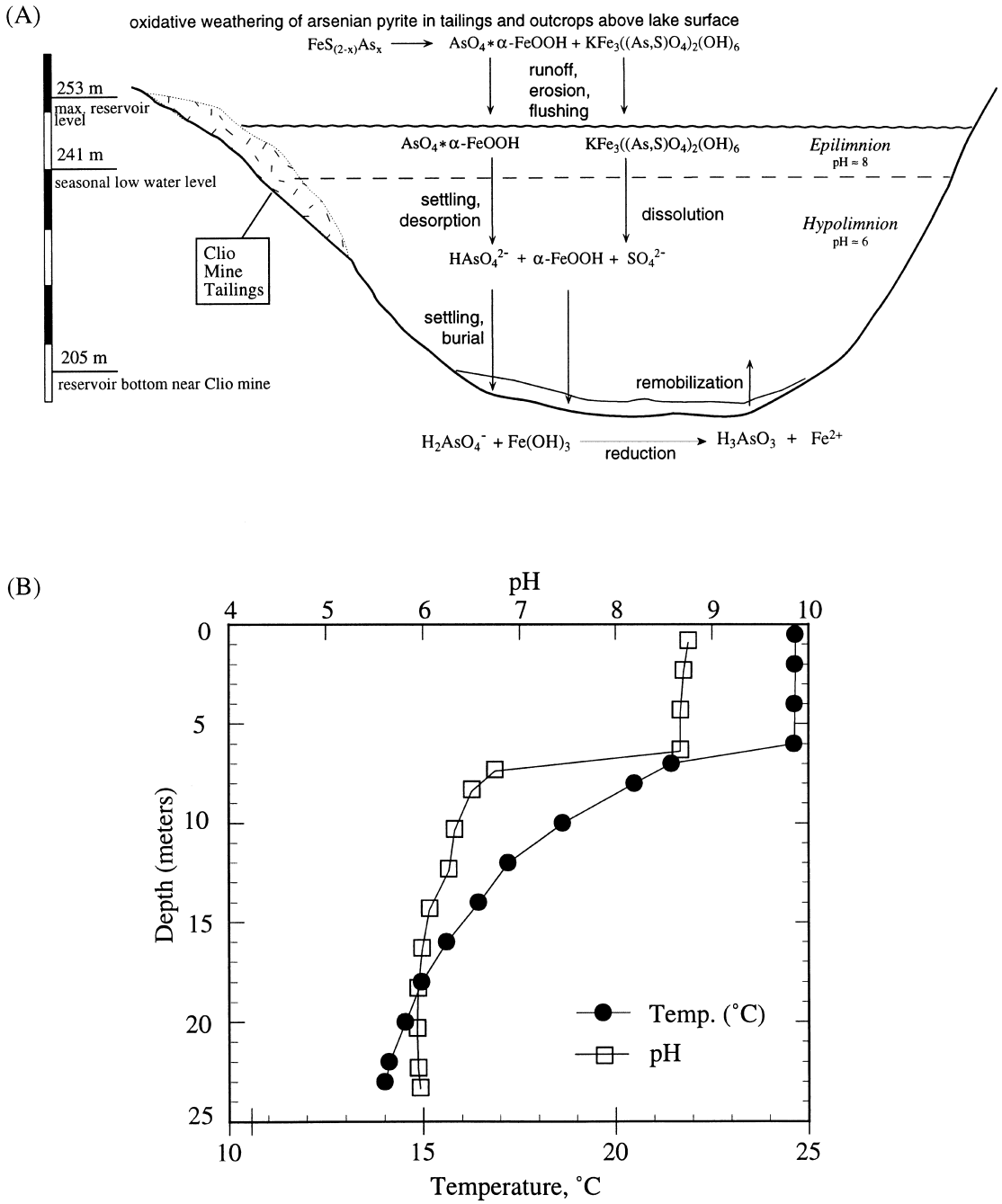

Fig. 9. (A) Schematic cross section of Don Pedro Reservoir showing simplified hydrogeochemical pathways of As. Seasonal rainfall erodes or dissolves As-bearing weathering products of arsenian pyrite, flushing them into the reservoir. Arsenate sorbed (or co-precipitated) on goethite desorbs under alkaline conditions. Arsenic-bearing jarosite releases As by dissolution or desorption. Iron and As settle into bottom sediments, where they may be remobilized upon reductive dissolution. Summer thermocline indicated by dashed line. (B) Temperature and pH profiles of Don Pedro Reservoir near the Clio Mine. Data collected August 1997 using a Hydrolab Minisonde Multiprobe^{TM}.

orb because maximum adsorption on goethite occurs below pH 6 (Manning and Goldberg, 1996). Filtered (0.45 μm) reservoir waters are supersaturated with respect to both ferrihydrite and goethite (Fe concentration 0.4 μM). Goethite particles or colloidal ferrihydrite flocs may settle to the lake bottom, introducing adsorbed As into the lake sediments (Crecelius, 1975; Chapman et al., 1983). Jarosite is not stable under the pH conditions of the reservoir mixis (Fig. 8) and is expected to dissolve, releasing associated As to lake waters. Thus, at the end of the winter rainy season, As in the reservoir will be distributed as (1) singly protonated As(V) [$HAsO_4^{2-}$] aqueous species; (2) adsorbed surface complexes on suspended goethite or ferrihydrite particles; and (3) adsorbed complexes on lake bottom sediments. Arsenic is expected to be strongly partitioned into the latter two environments.

By late spring/early summer, Don Pedro Reservoir becomes thermally stratified into a circulating, oxygenated, pH 8–9 epilimnion and a more reducing, noncirculating hypolimnion of pH ~6 (Point H in Fig. 8; Fig. 9). Fe oxyhydroxide particles that settle into the hypolimnion are no longer stable (Figs. 8 and 9), so adsorbed As is released when these phases dissolve. The predominant As species in the hypolimnion is expected to be fully protonated As(III) [H_3AsO_3] if thermodynamic equilibrium is achieved (Fig. 8); however, some metastable As(V) may remain. Arsenic adsorbed to Fe phases in the lake sediment is also subject to reduction. Abiotic and biotic reaction pathways (Cullen and Reimer, 1989; Dowdle et al., 1996) lead to Fe and As reduction following burial, reductively dissolving goethite or ferrihydrite and releasing thermodynamically stable As(III) or metastable As(V). The soluble reduced species will be released to sediment pore waters (Belzile and Tessier, 1990). Concentrations of As in sediment porewaters have been found to exceed those in overlying lake waters at other mine-impacted sites by a factor of up to 60 (Crecelius, 1975; Chapman et al., 1983). In anoxic waters, these concentration gradients drive upward diffusion of As (both As(III) and As(V)) into the lake water column, a process that is accelerated by sediment compaction (Aggett and O'Brien, 1985; Brannon and Patrick, 1987; Azcue et al., 1994). Hence As attenuated in sediments is remobilized and may be dispersed in the lake during the next winter mixis.

Mobilization of As from sulfide minerals into secondary weathering phases can adversely impact water supplies and aquatic life. An understanding of how As is sequestered in secondary phases and the environmental conditions under which it may be released to solution is required to predict the nature and extent of As distribution in aquatic systems. Geochemical information gathered at a range of scales from regional to molecular provides a powerful method for this type of assessment. This study has shown that in the Don Pedro Reservoir area of the California Mother Lode Gold District, As removed from arsenian pyrite during weathering is attenuated by either of two phases, goethite or jarosite, depending on the local buffering capacity of the pyrite-bearing rock. Goethite sequesters As by sorption, while jarosite primarily incorporates As into the mineral structure by substitution into the S site. The capacity of these minerals to retain As when transported into the lake environment depends on the seasonal pH and redox conditions within the reservoir. In general, goethite can retain adsorbed As except under reducing conditions of sediment burial and the summer hypolimnion, whereas jarosite is not stable under any reservoir conditions and can be expected to release As into the dissolved phase.

Acknowledgements

Discussions with Gordon E. Brown Jr., Mihaly Pósfai, Roger Ashley, and Andrea Foster were helpful in preparation of this manuscript. Charlie Alpers, Jim Rytuba, Mike Hunerlach and Roger Ashley were extremely helpful in guiding us through techniques for sample collection and trace element analysis, as well as for providing equipment and laboratory facilities. We thank Andrea Foster for scorodite and arsenopyrite EXAFS data, as well as for assistance in data collection; and John Bargar for providing a synthetic goethite sample. We thank Mihaly Pósfai and the staff of the HR-TEM laboratory at ASU for collection of the TEM data. We appreciate technical support from the staff of the Stanford Synchrotron Radiation Laboratory, from Bob Jones for assistance in microprobe analysis of silicates, and field assistance from Michael Parsons, Jim Sweeney, Phil Neuhoff, Thrainn Fridriksson and Patrick Redmond. SSRL is operated by the DOE, Office of Basic Energy Sciences. The SSRL Biotechnology Program is supported by the National Institutes of Health, National Center for Research Resources, Biomedical Technology Program, and by the DOE, Office of Biological and Environmental Research. Funding from the Stanford University Office of the Dean of Research Grant 127P047 (to DKB and TNT), the US Environmental Protection Agency "STAR" fellowship program and the Stanford School of Earth Science McGee and Shell Funds (to KSS), NSF Grant EAR-9902859 (to DKB) and NSF Grant EAR-9629276 (to PAO) is gratefully acknowledged.

This work began as a collaboration between Tracy Tingle and Dennis Bird, as they lounged about the campfire above one of Tracy's favorite kayaking rivers, the Tuolumne. The authors and many others have missed Tracy's enthusiasm for science and for adventure since his passing in 1996.

References

Aggett, J., O'Brien, G.A., 1985. Detailed model for the mobility of arsenic in lacustrine sediments based on measurements in Lake Ohakuri. Environ. Sci. Technol. 19, 231–238.

Alpers, C.N., Rye, R.O., Nordstrom, D.K., White, L.D., King, B.S., 1992. Chemical, crystallographic, and stable isotopic properties of alunite and jarosite from acid-hypersaline Australian lakes. Chem. Geol. 96, 203–226.

Azcue, J.M., Nriagu, J.O., Schiff, S., 1994. Role of sediment porewater in the cycling of arsenic in a mine-polluted lake. Environ. Internat. 20, 517–527.

Bayliss, P., 1989. Crystal chemistry and crystallography of some minerals within the pyrite group. Am. Mineral. 74, 1168–1176.

Belzile, N., Tessier, A., 1990. Interactions between arsenic and iron oxyhydroxides in lacustrine sediments. Geochim. Cosmochim. Acta 54, 103–109.

Bohlke, J.K., Kistler, R.W., 1986. Rb–Sr, K–Ar, and stable isotope evidence for the ages and sources of fluid components of gold-bearing quartz veins in the northern Sierra Nevada foothills metamorphic belt, California. Econ. Geol. 81, 296–322.

Bowell, R.J., 1994. Sorption of arsenic by iron hydroxides and oxyhydroxides in soils. Appl. Geochem. 9, 279–286.

Brannon, J.M., Patrick Jr, W.H., 1987. Fixation, transformation, and mobilization of arsenic in sediments. Environ. Sci. Technol. 21, 450–459.

Brown Jr, G.E., Parks, G.A., O'Day, P.A., 1995. Sorption at mineral-water interfaces: macroscopic and microscopic perspectives. Mineral. Soc. Ser. 5, 129–183.

Brown Jr, G.E., Calas, G., Waychunas, G.A., Petiau, J., 1988. X-ray absorption spectroscopy and its applications in mineralogy and geochemistry. Rev. Mineral. 18, 431–512.

Chapman, B.M., Jones, D.R., Jung, R.F., 1983. Processes controlling metal ion attenuation in acid mine drainage streams. Geochim. Cosmochim. Acta 47, 1957–1973.

Cherry, J.A., Shaikh, A.U., Tallman, D.E., Nicholson, R.V., 1979. Arsenic species as an indicator of redox conditions in groundwater. J. Hydrol. 43, 373–392.

Clark, L.A., 1960. The Fe–As–S system — phase relations and applications. Econ. Geol. 55, 1345–1381.

Crecelius, E.A., 1975. The geochemical cycle of arsenic in Lake Washington and its relation to other elements. Limnol. Oceanogr. 20, 441–451.

Cullen, W.R., Reimer, K.J., 1989. Arsenic speciation in the environment. Chem. Review 89, 713–764.

De Vitre, R., Belzile, N., Tessier, A., 1991. Speciation and adsorption of arsenic on diagenetic iron oxyhydroxides. Limnol. Oceanogr. 36, 1480–1485.

Dódony, I., Pósfai, M., Buseck, P.R., 1996. Structural relationship between pyrite and marcasite. Am. Mineral 81, 119–125.

Donovan, J.J., Tingle, T.N., 1996. An improved mean atomic number background correction for quantitative microanalysis. J. Microsc. Soc. Am. 2, 1–7.

Dowdle, P.R., Laverman, A.M., Oremland, R.S., 1996. Bacterial dissimilatory reduction of arsenic(V) to arsenic(III) in anoxic sediments. Appl. Environ. Microbiol. 62, 1664–1669.

Dutrizac, J.E., Jambor, J.L., 1987. The behavior of arsenic during jarosite precipitation: arsenic precipitation at 97 degree from sulfate or chloride media. Can. Metall. Q. 26, 91–101.

Dutrizac, J.E., Jambor, J.L., Chen, T.T., 1987. The behavior of arsenic during jarosite precipitation: reactions at 150 degree and the mechanism of arsenic precipitation. Can. Metall. Q. 26, 103–115.

Evangelou, V.P., Zhang, Y.L., 1995. A review: pyrite oxidation mechanisms and acid mine drainage prevention. Crit. Rev. Environ. Sci. Technol. 25, 141–199.

Fleet, M.E., MacLean, P.J., Barbier, J., 1989. Oscillatory-zoned As-bearing pyrite from strata-bound and stratiform gold deposits: An indicator of ore fluid evolution. In: Keays, R.R., Ramsay, W.R.H., Groves, D.I. (Eds.), The Geology of Gold Deposits: The Perspective in 1988, vol. 6, pp. 356–362.

Fleet, M.E., Chryssoulis, S.L., MacLean, P.J., Davidson, R., Weisener, C.G., 1993. Arsenian pyrite from gold deposits: gold and arsenic distribution investigated by SIMS and EMP, and color staining and surface oxidation by XPS and LIMS. Can. Mineral. 31, 1–17.

Foster, A.L., Brown Jr, G.E., Tingle, T.N., Parks, G.A., 1998. Quantitative arsenic speciation in mine tailings using X-ray absorption spectroscopy. Am. Mineral. 83, 553–568.

George, G.N., Pickering, I.J., 1993. EXAFSPAK: a suite of computer programs for analysis of X-ray absorption spectra. Stanford Synchrotron Radiation Laboratory.

Hansmann, D.D., Anderson, M.A., 1985. Using electrophoresis in modeling sulfate, selenite, and phosphate adsorption onto goethite. Environ. Sci. Technol. 19, 544–551.

Harrington, J.M., LaForce, M.J., Rember, W.C., Fendorf, S.E., Rosenzweig, R.F., 1998. Phase associations and mobilization of iron and trace elements in Coeur d'Alene Lake, Idaho. Environ. Sci. Technol. 32, 650–656.

Hem, J.D., 1977. Reactions of metal ions at surfaces of hydrous iron oxide. Geochim. Cosmoschim. Acta 41, 527–538.

Huffman, G.P., Huggins, F.E., Shah, N., Zhao, J., 1994. Speciation of arsenic and chromium in coal and combustion ash by XAFS spectroscopy. Fuel Process. Technol. 39, 47–62.

Huggins, F.E., Zhao, J., Shah, N., Lu, F., Huffman, G.P., Bool III, L.E., Senior, C.L., 1997. Investigation of the oxidation of arsenical pyrite in coal and its effect on the behavior of arsenic during combustion. DGMK Tagungsber. 9702, 381–384.

Kistler, R.W., Dodge, R.C.W., Silberman, M.L., 1983. Isotopic studies of mariposite-bearing rocks from the south-central Mother Lode, California. California Geology, 201–203.

Knopf, A., 1929. The Mother Lode system of California. US Geological Survey Professional Paper 157.

Koretsky, C.M., Sverjensky, D.A., Sahai, N., 1998. A model of surface site types on oxide and silicate minerals based on crystal chemistry: implications for site types and densities, multi-site adsorption, surface infrared spectroscopy, and dissolution kinetics. Am. J. Sci. 298, 349–438.

Kuhn, A., Sigg, L., 1993. Arsenic cycling in eutrophic Lake Greifen, Switzerland: influence of seasonal redox processes. Limnol. Oceanogr. 38, 1052–1059.

Landefeld, L.A., Snow, G.G., 1990. Yosemite and the Mother Lode Gold Belt; Geology, Tectonics, and the Evolution of Hydrothermal Fluids in the Sierra Nevada of California. In: Guidebook — Pacific Section, American Association of Petroleum Geologists, vol. 68.

Manceau, A., Boisset, M.-C., Sarret, G., Hazemann, J.-L., Mench, M., Cambier, P., Prost, R., 1996. Direct determination of lead speciation in contaminated soils by EXAFS spectroscopy. Environ. Sci. Technol. 30, 1540–1552.

Manning, B.A., Goldberg, S., 1996. Modeling competitive adsorption of arsenate with phosphate and molybdate on oxide minerals. Soil Sci. Soc. Am. J. 60, 121–131.

McMaster, W.H., Kerr Del Grande, N., Mallett, J.H., Hubbell, J.H., 1969. Compilation of X-ray cross sections. National Bureau of Standards.

Menchetti, S., Sabelli, C., 1976. Crystal chemistry of the alunite series: crystal structure refinement of alunite and synthetic jarosite: Neues Jahrb. Mineral. Monatsh. p. 406–117.

Moller, P., Kersten, G., 1994. Electrochemical accumulation of visible gold on pyrite and arsenopyrite surfaces. Mineral. Depos. 29, 404–413.

Morin, G., Ostergren, J.D., Juillot, F., Ildefonse, P., Calas, G., Brown, G.E.J., 1999. XAFS determination of the chemical form of lead in smelter-contaminated soils and mine talings: Importance of adsorption processes. Am. Mineral. 84, 420–434.

Nordstrom, D.K., Munoz, J.L., 1994. Geochemical Thermodynamics. Blackwell Scientific Publications, Boston.

O'Day, P.A., Carroll, S.A., Waychunas, G.A., 1998. Rock-water interactions controlling zinc, cadmium, and lead concentrations in surface waters and sediments, U.S. Tri-State Mining District — 1: molecular identification using X-ray absorption spectroscopy. Environ. Sci. Technol. 32, 943–955.

O'Day, P.A., Rehr, J.J., Zabinsky, S.I., Brown Jr, G.E., 1994. Extended X-ray absorption fine structure (exafs) analysis of disorder and multiple-scattering in complex crystalline solids. J. Am. Chem. Soc. 116, 2938–2949.

Ostergren, J.D., Brown Jr, G.E., Parks, G.A., Tingle, T.N., 1999. Quantitative speciation of lead in selected mine tailings from Leadville, CO. Environ. Sci. Technol. 33, 1627–1636.

Parsons, A.B., 1920. The mine and mill of the Belmont Shawmut Mining Co. Min. and Sci. Press 121, 619–624.

Pauling, L., 1978. Covalent chemical bonding of transition metals in pyrite, cobaltite, skutterudite, millerite and related minerals. Can. Mineral. 16, 447–452.

Peterson, M.L., Carpenter, R., 1986. Arsenic distributions in porewaters and sediments of Puget Sound, Lake Washington, the Washington coast and Saanich Inlet, B. C. Geochim. Cosmochim. Acta 50, 353–369.

Pierce, M.L., Moore, C.B., 1980. Adsorption of arsenite on amorphous iron hydroxide from dilute aqueous solution. Environ. Sci. Technol. 14, 214–216.

Pokrovsky, G., Gout, R., Schott, J., Zotov, A., Harrichoury, J.-C., 1996. Thermodynamic properties and stoichiometry of As(III) hydroxide complexes at hydrothermal conditions. Geochim. Cosmochim. Acta 60, 737–749.

Pontius, F.W., 1995. Uncertainties drive arsenic rule delay. J. Am. Water Works Assoc. 87, 12,150.

Pósfai, M., Buseck, P.R. 1997. Modular structures in sulfides: sphalerite/wurzite-, pyrite/marcasite-, and pyrrhotite-type minerals. In: Merlino, S. (Ed.), European Mineralogical Union Notes in Mineralogy, 1. Eotvos University Press, Budapest, pp. 193–235.

Pouchou, J.L., Pichoir, F. 1985. "PAP" $\phi\rho Z$ procedure for improved quantitative microanalysis. In: Armstrong, J.T. (Ed.), Microbeam Analysis. San Francisco Press, San Francisco, pp. 104–106.

Rattray, K.J., Taylor, M.R., Bevan, D.J.M., 1996. Compositional segregation and solid solution in the lead-dominant alunite-type minerals from Broken Hill, N.S.W. Mineral. Mag. 60, 779–785.

Rehr, J.J., 1993. Recent developments in multiple-scattering calculations of XAFS and XANES. Jpn. J. Appl. Phys., Part 1 32, 8–12.

Rehr, J.J., Albers, R.C., Zabinsky, S.I., 1992. High-order multiple-scattering calculations of X-ray-absorption fine structure. Phys. Rev. Lett. 69, 3397–3400.

Schwertmann, U., Fischer, W.R., 1973. Natural amorphous ferric hydroxide. Geoderma 10, 237–247.

Schwertmann, U., Cambier, P., Murad, E., 1985. Properties of goethites of varying crystallinity. Clays Clay Miner. 33, 369–378.

Scott, K.M., 1987. Solid solution in, and classification of, gossan-derived members of the alunite-jarosite family, northwest Queensland, Australia. Am. Mineral. 72, 178–187.

Seyler, P., Martin, J.-M., 1989. Biogeochemical processes affecting arsenic species distribution in a permanently stratified lake. Environ. Sci. Technol. 23, 1258–1263.

Szytula, A., Burewicz, A., Dimitrijevic, Z., Krasnicki, S., Rzany, H., Todorovic, J., Wanic, A., Wolski, W., 1968. Neutron diffraction studies of alpha -FeOOH. Physica Status Solidi 26, 429.

Thanabalasingam, P., Pickering, W.F., 1986. Effect of pH on interaction between As(III) or As(V) and manganese(IV) oxide. Water, Air Soil Pollut. 29, 205–216.

Van Geen, A., Robertson, A.P., Leckie, J.O., 1994. Complexation of carbonate species at the goethite surface: implications for adsorption of metal ions in natural waters. Geochim. Cosmochim. Acta 58, 2073–2086.

Wagner, J.R., 1970. Gold Mines of California. University of California Press, Berkeley.

Walker, W.J., Galleni, A.M., Dragoo, J.P., 1994. Arsenic speciation and solubility in mine tailings from Mesa de Oro, California: Sacramento, CA, Science and Engineering Analysis Corporation (SEACOR).

Waychunas, G.A., Fuller, C.C., Rea, B.A., Davis, J.A., 1996. Wide angle X-ray scattering (WAXS) study of "two-line" ferrihydrite structure: effect of arsenate sorption and counterion variation and comparison with EXAFS results. Geochim. Cosmochim. Acta 50, 1765–1781.

Waychunas, G.A., Rea, B.A., Fuller, C.C., Davis, J.A., 1993. Surface chemistry of ferrihydrite — Part 1: EXAFS studies of the geometry of coprecipitated and adsorbed arsenic. Geochim. Cosmochim. Acta 57, 2251–2269.

Weir, R.H.J., Kerrick, D.M., 1987. Mineralogic, fluid inclusion, and stable isotope studies of several gold mines in the Mother Lode, Tuolumne and Mariposa Counties, California. Econ. Geol. 82, 328–344.